



THE HONG KONG  
POLYTECHNIC UNIVERSITY

香港理工大學

Pao Yue-kong Library

包玉剛圖書館

---

## Copyright Undertaking

This thesis is protected by copyright, with all rights reserved.

**By reading and using the thesis, the reader understands and agrees to the following terms:**

1. The reader will abide by the rules and legal ordinances governing copyright regarding the use of the thesis.
2. The reader will use the thesis for the purpose of research or private study only and not for distribution or further reproduction or any other purpose.
3. The reader agrees to indemnify and hold the University harmless from and against any loss, damage, cost, liability or expenses arising from copyright infringement or unauthorized usage.

### IMPORTANT

If you have reasons to believe that any materials in this thesis are deemed not suitable to be distributed in this form, or a copyright owner having difficulty with the material being included in our database, please contact [lbsys@polyu.edu.hk](mailto:lbsys@polyu.edu.hk) providing details. The Library will look into your claim and consider taking remedial action upon receipt of the written requests.

Pao Yue-kong Library, The Hong Kong Polytechnic University, Hung Hom, Kowloon, Hong Kong

<http://www.lib.polyu.edu.hk>

**The Hong Kong Polytechnic University**

**Department of Applied Physics**

**Electrosynthesis of oxide films on flexible  
plastics**

**Wong Ching Hong**

**A thesis submitted in partial fulfillment of the requirements  
for the degree of Master of Philosophy**

**September 2010**

## **CERTIFICATE OF ORIGINALITY**

I hereby declare that this thesis is my own work and that, to the best of my knowledge and belief, it reproduces no material previously published or written, nor material that has been accepted for the award of any other degree or diploma, except where due acknowledgement has been made in the text.

\_\_\_\_\_ (Signed)

\_\_\_\_\_ Wong Ching Hong \_\_\_\_\_ (Name of student)

## Abstract

Transparent zinc oxide (ZnO) films on flexible copper-coated polyethylene terephthalate (PET) sheet have been grown by a potentiostatic cathodic deposition technique using aqueous zinc nitrate as the electrolyte. In this project, different deposition parameters such as applied cathodic potential, concentration of electrolyte and bath temperature had been used to fabricate the ZnO films. Their structural and optical properties were characterized by X-ray diffractometer (XRD), scanning electron microscope (SEM), diffuse reflectance UV-VIS spectrophotometer and photoluminescence (PL) spectrometer. On the basis of our measurements, the effects of different deposition parameters on the structural and optical properties of the ZnO films have been revealed. Furthermore, we demonstrated that high quality ZnO films have been successfully grown on flexible polymeric substrates using a low temperature potentiostatic cathodic deposition technique.

Apart from ZnO films, cuprous oxide ( $\text{Cu}_2\text{O}$ ) films were deposited on flexible copper-coated PET substrates using potentiostatic cathodic deposition technique. The electrolyte used in fabricating the  $\text{Cu}_2\text{O}$  films was a mixture of copper(II) sulphate, lactic acid and sodium hydroxide. Similar to ZnO films, the effects of processing parameters such as applied cathodic potential and deposition time on the structural,

electrical and optical properties of the deposited  $\text{Cu}_2\text{O}$  films were investigated.

Well-defined polycrystalline  $\text{Cu}_2\text{O}$  was electrodeposited on metalized PET substrates.

Finally, experimental conditions, for example, deposition voltage and temperature of the deposition solution were especially important in controlling the morphology of the deposited ZnO on  $\text{Cu}_2\text{O}$  film. In this thesis, a mechanism for the deposition process has been proposed based on our experimental results. Based on the optimal processing parameters for ZnO as well as  $\text{Cu}_2\text{O}$  films, heterojunctions of ZnO/ $\text{Cu}_2\text{O}$  on Cu-coated PET structure were fabricated. Their electrical properties were measured. The photovoltaic properties of the ZnO/ $\text{Cu}_2\text{O}$  heterostructure were demonstrated by our electrical measurements. XRD and SEM were employed to characterize the structure and surface morphology of the  $\text{Cu}_2\text{O}$  films respectively. The optical absorption was measured by a transmission UV-VIS spectrometer.

# Publication

1. *Ching Hong Wong, Chee Leung Mak, Kin Hung Wong, Potentiostatic Deposition of Zinc Oxide on Flexible Substrate, 5th FORUM ON NEW MATERIALS PART D, pp43-48*

# Acknowledgements

This research has been carried out for the past two years at The Hong Kong Polytechnic University. Many people have given helps and guidance to the author during the course of this research work. The authors would like to thank Dr. C. L. Mak (Department of Applied Physics) and Prof. K. H. Wong (Department of Applied Physics), for their supervision guidance, encouragement, suggestions and information.

The author would also like to express his gratitude to Dr. W.L. Sin and Dr. M. Zhang for their encouragements to the author during his work at The Hong Kong Polytechnic University. The author would like to thank all the staff members in the Department of Applied Physics and Materials Research Center at the Hong Kong Polytechnic University.

The financial support from the Research Committee of the Hong Kong Polytechnic University, which was essential for the author's graduate studies, is acknowledged.

# Table of contents

Abstract.....	i
Publication .....	iii
Acknowledgements .....	iv
Table of contents.....	v
List of figures .....	viii
Chapter 1 Introduction.....	1
1.1 Background.....	1
1.2 History of development of solar cell and photovoltaics .....	2
1.3 Develop of flexible electronic device .....	5
1.4 Development of electrodeposition of semiconductors.....	8
1.5 Objective .....	12
Chapter 2 Literature Review .....	15
2.1 Zinc Oxide (ZnO).....	15
2.2 Cuprous Oxide (Cu <sub>2</sub> O).....	18
2.3 Theories of Electrodeposition .....	20
2.4 Cyclic voltammetry.....	27
2.5 Mott-Schottky Plot.....	30
2.6 Photoelectrochemical measurement.....	32
2.7 X-Ray Diffraction .....	34
2.8 Scanning Electron Microscopy .....	37
2.9 Electrical measurement.....	38
2.10 Schottky contact.....	43
2.11 Ultraviolet-Visible spectroscopy.....	46
2.12 Photoluminescence spectroscopy.....	49

Chapter 3 Experimental section .....	52
3.1 Substrates preparation .....	52
3.2 Electrodeposition of metal oxide .....	52
3.2.1 Zinc Oxide .....	53
3.2.2 Cuprous Oxide .....	54
3.2.3 Hetero-junction of Zinc Oxide/Cuprous Oxide .....	55
3.3 Photoelectrochemical studies .....	56
3.4 Mott-Schottky plot .....	56
3.5 X-ray diffraction .....	56
3.6 Scanning Electron Microscopy .....	57
3.7 UV-VIS spectroscopy .....	57
3.8 Photoluminescence spectroscopy .....	57
3.9 Electrical Characterization .....	58
3.10 Atomic force microscopy .....	59
Chapter 4 Results and Discussions .....	60
4.1 Zinc Oxide .....	60
4.1.1 Electrodeposition .....	60
4.1.2 Structural Properties .....	69
4.1.3 Optical Properties .....	74
4.1.4 Electrical Properties .....	82
4.2 Cuprous Oxide .....	84
4.2.1 Electrodeposition .....	84
4.2.2 Structural Properties .....	90
4.2.3 Optical Properties .....	96
4.2.4 Electrical Properties .....	98
4.3 Hetero-Junction of Zinc Oxide / Cuprous Oxide .....	102

4.3.1 Electrodeposition.....	102
4.3.2 Structural Properties.....	103
4.3.3 Optical Properties .....	105
4.3.4 Electrical Properties .....	106
Chapter 5 Conclusion .....	108
Reference .....	110

## List of figures

Figure 1	The development of solar cells.....	4
Figure 2	Stick and ball representation of ZnO crystal structures: (a)cubic rocksalt ( <i>B1</i> ), (b)cubic zinc blende ( <i>B3</i> ), and (c) hexagonal wurtzite ( <i>B4</i> ).The shaded gray and black spheres denote Zn and O atoms, respectively. ....	17
Figure 3	Schematic representation of a wurtzitic ZnO structure having lattice constants $a$ in the basal plane and $c$ in the basal direction; $u$ parameter is expressed as the bond length or the nearest-neighbor distance $b$ divided by $c$ (0.375 in ideal crystal), and $\alpha$ and $\beta$ ( $109.47^\circ$ in ideal crystal) are the bond angles.....	18
Figure 4	Drawings of the cuprous oxide ( $\text{Cu}_2\text{O}$ ) structure type emphasizing (left) the relation to antifluorite structure type and (right) the extended lattice demonstrating the diamond-like lattice connectivity. Copper atoms are drawn in blue and oxygen atoms in red. ....	20
Figure 5	Types of electrical driving forces (current or potential). (a) Direct current .....	23
Figure 6	Approximate regions in which various stages of ion transport occur leading to electrodeposition, .....	24
Figure 7	Potential-time signal in cyclic voltammetry experiments[38]. ....	28
Figure 8	Typical cyclic voltammogram for a) a reversible $\text{O} + n\text{e} \rightleftharpoons \text{R}$ redox processes and b) irreversible processes. $E_{p.c.}$ and $E_{p.a.}$ represents the cathodic peak and anodic peak current, respectively [37]. ....	29
Figure 9	Gaussian x-ray diffraction peak profile. ....	36
Figure 10	Bulk resistance and its geometrical dimensions .....	39

Figure 11 A typical symmetric current-voltage (i-v) characteristic of a metal-semiconductor-metal structure.....42

Figure 12 Formation of a Schottky contact. a) Situation if there is no contact between the metal and the n-type semiconductor. b) Hypothetical situation if the materials would be brought suddenly into contact. No surface states that might pin the  $E_F$  are assumed. For clarity, any possible hole concentration is neglected. ....43

Figure 13 Schottky contact in thermal equilibrium. There is a layer of electrons in the metal .....44

Figure14 Schematic diagram of the band structure of semiconductors. ....47

Figure 15 Photoluminescence schematic. (a) An electron absorbs a photon and is promoted from the valence band to the conduction band. A electron-hole pair is generated (b) The electron cools down to the bottom of the conduction band. (c) The electron recombines with the hole resulting in the emission of light with energy  $h\nu$ . ....50

Figure 16 The schematic setup for electrodeposition experiment.All the mentioned voltages in voltage scanning and electrodeposition are the results of cathode versus the reference electrode (Ag/AgCl with saturated KCl) but not anode. ....52

Figure17The schematic structure of the layer-by-layer ZnO/Cu<sub>2</sub>O heterojunction . ....55

Figure 18 Schematic diagram illustrates the contact points for the ZnO/Cu<sub>2</sub>O heterojunction. ....58

Figure 19 Cyclic voltammogram of a Cu coated PET electrode in 0.01M zinc nitrate solution with bath temperature: 80°C and pH: 3.6 . ....60

Figure 20 Effect of concentration on the cyclic voltammogram.....61

Figure 21	Effect of temperature on the cyclic voltammogram .....	63
Figure 22	Chronoamperometric transient curves of the effect of a) applied voltage, b) concentrations and c) temperature. ....	65
Figure 23	X-ray theta-2 theta scans of the prepared ZnO films. (* represents the diffraction peaks from Cu-coating.).....	69
Figure 24	SEM micrographs of the ZnO films prepared by varying deposition potentials, bath concentration and bath temperature (from left to right): sample A to C (first row), sample D and sample E (second row), sample F and sample G (third row).....	71
Figure 25	AFM micrographs of ZnO thin films deposited on Cu-coated PET (sample D).....	73
Figure 26	Photoluminescence spectra of (a) samples A, B and C (varying cathodic deposition voltage) (b) samples B, D and E (varying deposition bath concentration) and (c) samples D, F and G (varying deposition temperature). ....	75
Figure 27	Photoluminescence spectra of (a) sample B, (b) sample D and (c) sample F. Red lines: Gaussian fitting for each curve. ....	76
Figure 28	Diffuse UV-Vis reflectance spectrum and Kubelka-Munk transformed reflectance spectrum (inset) of deposited ZnO film on Cu-coated PET (sample D). ....	81
Figure 29	Mott-Schottky plots of ZnO in sample D. Solid lines represent the fits of the experimental data employing Eq.2.6, and the dashed line represents the fitting curve. $E_{we}$ is the voltage between the reference electrode (Ag/AgCl in sat' KCl) and the voltage of working electrode. ....	82
Figure 30	Voltammogram on copper-coated PET in 0.45 M $CuSO_4$ , 3.25M	

lactic acid and NaOH. Scanned rate is 20 mV s <sup>-1</sup> , pH is 10.0 and temperature is 40°C.....	84
Figure 31 Chronoamperometric transient curves of the effect of a) applied voltage of sample 1 to 3, b) applied voltage of sample 4 to 6 and c) deposition time.....	88
Figure 32 XRD patterns of Cu <sub>2</sub> O films deposited at: (a) various applied cathodic potentials, sample 1 to sample 6; (b) different deposition times, sample 7 to sample 9. (* represents the diffraction peaks from Cu-coating.) .....	90
Figure 33. SEM micrographs of the Cu <sub>2</sub> O films prepared by varying the deposition potentials. ....	93
Figure 34 SEM micrographs of the Cu <sub>2</sub> O films prepared by different deposition time.....	95
Figure 35 Absorbance of UV-VIS measurement on a) sample 1, b) sample 3 and c) sample 9. Insets show the Kubelka-Munk transformed reflectance spectrum of each sample. ....	97
Figure 36 The current-voltage curve of the sample 1 and sample 3. ....	98
Figure 37 Current-potential characteristics for a Cu <sub>2</sub> O layer of sample 3 under and without illumination in 0.5 M NaHCO <sub>3</sub> solution.....	101
Figure 38 a) cyclic voltammogram of a Cu <sub>2</sub> O film electrode (sample 1 was used) in 0.1M zinc nitrate bath with bath temperature of 80°C and pH of 3.6. b) current transient curve during the potentiostatic deposition at -0.55V.....	102
Figure 39 XRD patterns of sample 1 before (upper) and after (lower) the fabrication of a ZnO layer on it.....	103
Figure 40 The SEM image shows the surface of the ZnO electrodeposited	

on cuprous oxide layer (left) and the sample 1 (right).....	104
Figure 41 The UV-VIS reflectance of the ZnO/Cu <sub>2</sub> O sample represents in terms of absorbance versus the wavelength.....	105
Figure 42 The current-voltage curve of the deposited ZnO/Cu <sub>2</sub> O heterojunction. ....	106
Figure 43 Band diagrams of the isolated states (a) and the junction of ZnO and Cu <sub>2</sub> O (b).[64, 66] $E_C$ , $E_V$ and $E_F$ are the conduction-band-edge, valence-band-edge and Fermi-level, respectively.....	107

# Chapter 1 Introduction

## 1.1 Background

With continuous reduction of fossil fuel resources and more and more stringent restrictions for greenhouse gas emissions, human ever-increasing demand for energy forces people to seek highly effective inexhaustible energy sources.

The main source of our world's electricity is from burning of fossil fuel. This process releases huge amount of CO<sub>2</sub>, a greenhouse gas which is a suspected main contributor to the global warming. Furthermore, the recent high crude oil price promotes the exploration of alternative energy sources. Therefore, different kinds of renewable energy have been investigated and set to increase the share. The major concern of the green electricity is their cost. A competitive cost of the green electricity against the oil price is always attractive. Solar energy, with many advantages such as large reserve, sustainable utilization, environment-friendly nature, is no doubt the preferred and optimal. Converting sunlight into electricity is one way to effectively use solar energy, because electricity is the basic input form of energy for most energy-consuming equipment and has superior advantages for long-range transmission, easy storage etc. Solar cells, devices to convert solar energy to electrical one, have been developing

very rapidly both in industry and research.

## **1.2 History of development of solar cell and photovoltaics**

The working principle of inorganic solar cells is based on the photovoltaic effect occurred at a p–n junction. By contacting n-type and p-type semiconductors together, a p–n junction at their interface is formed. A space charge area closed to the interface is formed due to the diffusion of majority carriers. A built-in electric field directing from the n-type region to the p-type region is developed. Then, drifting of the majority carriers grows in the reverse direction. Finally, the system reaches equilibrium so that the current produced by diffusion equals to that produced by drifting. When light with energy higher than the band gap energy of the materials is illustrated at the p–n junction, electron–hole pairs are generated in the vicinity of the p–n junction. Non-equilibrium charge-carriers will diffuse toward both ends of the space-charge region due to this built-in electric field. Hence, light-induced electric potential is created and this results in destruction of the original balance. When the external electric circuit is completed by connecting electrodes on both sides of the cell with a load, an available electric power can be obtained.

Inorganic materials such as silicon, cadmium sulfide (CdS) and copper indium

gallium selenide (CIGS) have been developed for the fabrication of thin film photovoltaics rapidly since 70s of the 20<sup>th</sup> century. However, the development of silicon solar cells was hindered due to several great technical challenges such as high expense, great difficulty in producing high quality silicon films on large non-silicon substrate and needs of high-temperature-resistance substrates to endure a long heat treatment. Unlike silicon, the structure of other semiconductor solar cells such as CIGS is a more complex heterojunction system. Although some of the power conversion efficiencies of these solar cells can achieve around 20%, the development of these compound semiconductor solar cells are still limited by problems such as limited reserves of elements including indium, gallium and selenium, difficulty in preparing high-purity semiconductor materials, high cost of fabrication and so on.

Various solar cells have been fabricated in different laboratories (Figure 1)[1, 2].

Besides the traditional silicon cells, multi-junction and thin film technologies using conducting oxides, such as copper indium gallium diselenide [Cu(In,Ga)Se<sub>2</sub>] and cadmium telluride [CdTe], are the newest trend.

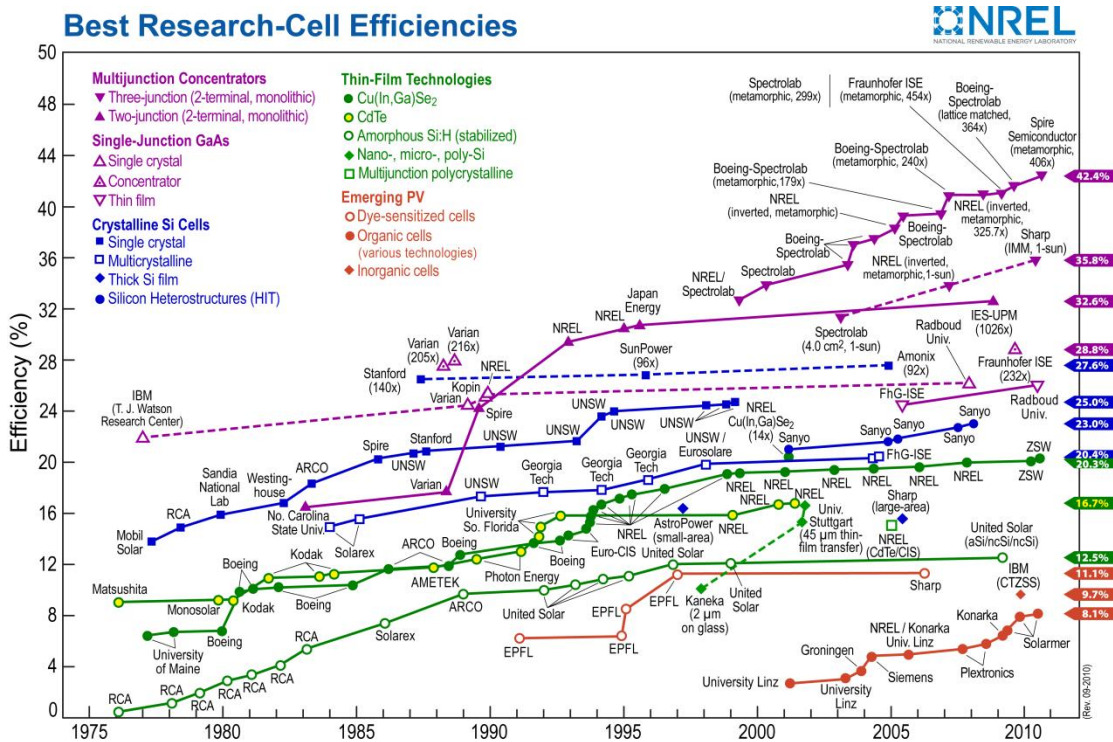


Figure 1 The development of solar cells.

However, the purification of Si from SiO<sub>2</sub> using popular Czochralski or Siemens process is very expensive. More important, they consume lot of energy for heating the materials during the fabrication process.

Dye-sensitized solar cells (DSSCs) and organic photovoltaic cells (OPV) have become the two hot spots of concern over the past two decades. As the mechanism of electron-carriers (or so called excitons) generation is totally different from that of the inorganic solar cell, this brings the development of photovoltaic cells into a new era. Besides possessing advantages of being a simple and low production cost method, non-toxicity, high power conversion efficiency even under weak light and capable of growing on flexible substrates, DSSC and OPV are still

limited by their encapsulation and the long-term stability of the photoactive materials.

As a result, flexible organic cells still face the challenges of low visible light absorption, photochemical stability[3] and, most importantly, long-term outdoor stability. Hence, it is still necessary to develop high quality inorganic photovoltaic films for solar cells applications.

### **1.3 Develop of flexible electronic device**

Beyond the traditional application of solar panels for large scale power station, the most attractive application of solar cell is their potential for small aircrafts, cars and various portable electric devices. As these solar cells benefit from the simple setup and direct current generation, light-weighted and flexible solar cells are demanded in order to suit different missions such as spaceship for deep-space missions, integration of photovoltaics with textiles, architectural fabrics and so on.

In 1967, the idea of flexible solar cell was proposed by reducing the thickness of the silicon films in order to be successfully grown on a flexible plastic substrate. However, with the limitation of the thin film processing techniques at that time, no great improvement had been achieved for many years. In 2008, after more than four decades,

Rogers and co-workers [4] successfully made a scalable, deformable and foldable integrated circuit by applying transfer printing technology to monocrystalline silicon nanoband array. This study showed that either amorphous or polycrystalline silicon is able to be fabricated as a flexible solar cell.

For the fabrication of flexible solar cells, thin film technologies are playing an important role. Current thin-film solar cells consist of few very thin layers that are continuous in two dimensions. By fabricating these thin layers on flexible substrates, these cells can be bent but do not crinkle. Transfer-printed method, which is one of the commonly used production processes, can deposit solar materials onto the substrate. However, based on this technique, areas of the devices are limited as it is difficult to scale-up the equipment. Thus, a new developed technique which can be easily scale up for industrial application will be of paramount importance.

Apart from the processing technique, flexible substance is also very important for the development of flexible electronic devices. Flexible metal sheets (stainless steel and molybdenum, etc.) and polymers (polyimide, etc.) are commonly employed as substrates for flexible electronic devices. Although metal sheets are capable of high deposition temperature which is beneficial to active layer deposition, they aggravate

diffusion of impurities from the substrate towards the active layer. Therefore, an electrical insulating layer is necessary on top of the substrate in order to block the diffusion between the substrate and the active layer. Polymer substrates are also used as flexible substrates to replace glass substrates. In order to be an ideal substrate, these polymers should possess good optical, mechanical and chemical properties. General speaking, polymers have high optical transparency, good mechanical as well as chemical stabilities, good chemical erosion resistance, low thermal expansion coefficient, smooth surface, and anti-air as well as anti-water permeability. Among various polymers, polyester, polycarbonate and polyimide are the candidates. For being a good substrate for devices, the heat-resistance of the polymer substrate is also an issue. For instance, polyethylene terephthalate (PET) sheet which is a kind of commonly used substrate material, has a relative high heat resistance with its highest thermal stability temperature of about 150 °C. Although this 150 °C is relatively higher than many polymers, the processing temperature used in the devices fabrication, especially for process of heat-sintering and annealing, will be yet limited by this thermal stability temperature. Due to the low-process temperature, films of low crystallinity are usually obtained by using common physical deposition methods. In this case, the efficiency of the whole devices drop intensively. [5],[6] Therefore, a low processing temperature technique will be needed to deposit inorganic films on PET

substrates for flexible solar cell applications.

## **1.4 Development of electrodeposition of semiconductors**

Electrodeposition of single elements such as gold and silver has been used for centuries in extraction of metals from their natural ores and electroplating of jewelry. However, electrodeposition of semiconducting materials is relatively new and was first introduced in the late 1970s.[7],[8] In the early 1980s', thin film CdS/CdTe solar cells with efficiency greater than 10% were developed based on the electrodeposited CdTe layer[9]. This work stimulated worldwide research interests in electrodeposition of semiconductors. Researches focused in the past two decades have not been just limited to II-VI semiconductors, but also on many other materials such as III-V, I-III-VI<sub>2</sub>, and other alloy semiconductors. Furthermore, elemental semiconductors such as silicon[10] as well as mechanically harder materials such as nitrides have been successfully grown by electrodeposition.[11]

The development of thin film electronics normally suffers from high production cost. For example, a well-established molecular beam epitaxy (MBE) system or metal organic chemical vapor deposition (MOCVD) system needs an initial cost in the order of £1 million. These systems also have limitations on the number of different

materials that can be grown. In comparison, a computerized potentiostat costs only about £5000 and a wide range of materials can be grown. Changing the electrolytic cell provides the conditions necessary for the growth of a new material. Other current established techniques for fabrication of ceramic thin films include pulsed laser deposition, rf sputtering, electron beam etching, metal-organic chemical vapor deposition, and molecular beam epitaxy.[12-16] Most of these techniques involve a two-step process. In the first step, the desired ceramic material is synthesized in bulk by any of the known conventional methods. In the second step, the pressed ceramic pellet is used as the target and is irradiated by a high-power laser, an ion electron beam, or a rf source. The resultant plume is captured onto a cold substrate. These techniques usually require a high power source and/or an ultrahigh vacuum system, making them extremely capital and energy intensive. Furthermore, these techniques are inapplicable when the substrate material is a low-temperature phase, as the plume would lead to instantaneous decomposition of the substrate material. Hence, there is an urgent need to develop a simple and inexpensive process to fabricate conducting oxide films on polymer substrates.

Similar to electrodeposition of metal, electrodeposition of semiconductor requires an electrolyte containing appropriate ions and three electrodes. In addition, an extrinsic

doping can be easily applied by adding calculated amounts of dopants into the electrolyte. Intrinsic doping also is possible by varying the composition of the electrolyte. Meanwhile, both doping approaches can tune the bandgap of the semiconductors which can be measured by conventional optical absorption.

In general, most of the physical deposition methods involve gas-to-solid phase changes during the growth process. However, in electrodeposition, phase change a liquid-to-solid occurs, and nature usually prefers this transition.[17] Thus, electrodeposition should produce high-quality material layers. In addition, the high potential gradient of  $10^5 \text{ V cm}^{-1}$  at the cathode surface within the electric double layer provides a good growth condition. This also leads to products which cannot be obtained in a chemical synthesis on substrates of any shape, fulfilling the charge neutrality requirements during the growth process. Another nice feature of this electrochemical synthesis is that it is a low-temperature technique with operation temperature lower than the boiling point of the electrolyte. Since the electrolyte used in our experiment is water-base, thus the operation temperature is below  $100^\circ\text{C}$ .

The principle of electrochemical synthesis is based on an oxidation or a reduction reaction of the species in the electrolyte. By fine-tuning the applied cell potential, the

oxidizing or reducing power can be continuously varied and suitably selected. Therefore, thermodynamic control can be exercised. This process is called potentiostatic synthesis which yields a pure single-phase product. However, current usually decays rapidly as the reaction proceeds due to low rates of diffusion of the reactant and decrease in activity of the reactant. Other than thermodynamic control, kinetic control can be exercised by adjusting the current passed through the cell to perform galvanostatic synthesis which leads to films with good adhesion and a controlled morphology, but a multiplicity of products may present in the deposit as cell potential drifts.

Types of electrosynthetic techniques and the nature of products obtained from each technique are listed in Table 1. [18]

Table 1. Summary of the Electrosynthetic Techniques Employed in Inorganic Solid-State Chemistry

Technique	Product	application
1. electromigration of reactant species	polycrystalline powders/ single crystals	battery electrode materials
2. electrolysis of fused salts	single crystals	crystal growth at moderate temperature
3. electrogeneration of base by cathodic reduction	coatings/films/powders	synthesis of electrode materials for secondary cells, fabrication of hydroxide films/coatings
4. anodic oxidation	coatings/films/powders	synthesis of compounds with high oxidation state
5. alternate current synthesis	layer-by-layer films/coatings	synthesis of composites/solid solutions

## 1.5 Objective

Energy conversion using photovoltaic devices is a one-step conversion process which generates electrical energy directly from sun light. Of course, solar cells of high efficiency and low cost are always desired. However, recent developments of solar cell mainly focus on realization of high light–electricity conversion efficiency, and as a result, the cost, fabrication complexity and longevity of the solar cells are relatively being disregarded. Indeed, fabrication of solar cells with low cost per watt is also of

paramount important for the needs of large scale solar electricity generation.

In order to produce solar cells of low cost, fabrication process should be simple and effective. Among various fabrication methods, electrosynthesis method is a potential candidate for the development of cost-oriented solar cells. Apart from the fabrication process, materials are also indispensable in the development of these low cost solar cells. In this project, inexpensive, stable and direct bandgap PV materials, based on metallic oxide films grown on flexible substrate, will be used in order to produce a low cost solar cell.

In this thesis, systematic investigation of the structural, surface morphology, optical and electrical properties of the as-deposited zinc oxide and cuprous oxide films grown by cathodic potentiostatic deposition method were performed. For the zinc oxide films, effects of processing parameters such as applied cathodic potential, bath concentration and bath temperature on the structural, electrical and optical properties were studied. For the  $\text{Cu}_2\text{O}$  films, applied cathodic potential and deposition time on the structural, electrical and optical properties were investigated. Finally, a hetero-junction was formed by electrodepositing a ZnO layer on  $\text{Cu}_2\text{O}$  film grown on Cu-coated PET substrates using the optimized condition obtained before. The structural, electrical and

optical properties of the heterojunction were investigated.

## Chapter 2 Literature Review

### 2.1 Zinc Oxide (ZnO)

Zinc oxide (ZnO) has been featured as subject of thousands of research papers, it can be traced the history back as early as 1935 [19]. ZnO has many distinct properties such as high ultra violet absorbance, wide chemistry, large piezoelectricity and strong luminescence at high temperatures. All these unique properties make ZnO being popular in industrial applications. It can be found in paints, cosmetics, plastic and rubber manufacturing, electronics and pharmaceuticals, and so on. ZnO is one of the transparent conductive oxides (TCOs) which are indispensable materials used as electrodes for optoelectronic devices such as flat panel displays and solar cells.

ZnO possesses a wide and direct bandgap of 3.3 eV and a large exciton binding energy of 60 meV at room temperature. It is a II-VI compound semiconductor whose ionicity resides at the borderline between covalent and ionic semiconductors. The crystal structures of ZnO are wurtzite (*B4*), zinc blende (*B3*), and rocksalt (*B1*), as schematically shown in Figure 2. At ambient conditions, the thermodynamically stable phase is wurtzite. The zinc-blende ZnO structure is stabilized only by growing on cubic substrates, and the rocksalt (NaCl) structure is obtained at relatively high

pressures[20]. The wurtzite structure has a hexagonal unit cell with two lattice parameters,  $a$  and  $c$ , in the ratio of  $c/a = 1.633$  and belongs to the space group of  $C_{6v}^4$  or  $P6_3mc$ . The lattice constants are  $3.25 \text{ \AA}$  and  $5.20 \text{ \AA}$  for the  $a$  and  $c$  parameters respectively. Indeed, the  $c/a$  ratio and  $u$  parameter can vary in a slightly wider range, from 1.593 to 1.604 and from 0.383 to 0.3856, respectively. Here  $u$  parameter is defined as the bond length or the nearest neighbor distance divided by  $c$ . On the other hand, for the zinc-blende polytype ZnO, the theoretical lattice constants based on a modern *ab initio* technique is predicted to be  $4.60 \text{ \AA}$ . Moreover, a high-pressure phase transition from the wurtzite to the rocksalt structure decreases the lattice constant down to  $4.271 \text{ \AA}$ .

Photocurrent is generated by irradiating ZnO with light of wavelength below 375 nm. As a result, ZnO holds excellent promise for blue and ultra-violet optical devices. In photovoltaic devices, ZnO is normally used as an n-type window layer in the thin film solar cells based on p-n junctions or dye sensitized solar cells [21]. A high optical transparent wurtzite ZnO film has been prepared by cathodic deposition from a simple zinc nitrate [ $\text{Zn}(\text{NO}_3)_2$ ] aqueous solution [22].

Inherent defect centres, such as oxygen vacancies and zinc interstitials are believed to

be responsible for the visible photoluminescence observed in ZnO. [23] Markevich et al. [23] showed that recombination centers responsible for the orange band were the centers of photosensitivity. Defects in ZnO strongly depend on the preparation and annealing conditions which in turn affect the photoconduction properties.

In recent years, urgent development of alternatives to tin-doped indium oxide (ITO), a superior transparent conducting oxide (TCO) in terms of fabrication, electrical conductivity, and etching characteristics, is needed because the material cost of indium, a quite expensive rare metal element, is increasing. A transparent conductive ZnO film is one of the candidates that find numerous applications in electronics and optical devices due to their suitable electrical, optical as well as acoustic characteristics and low material cost.

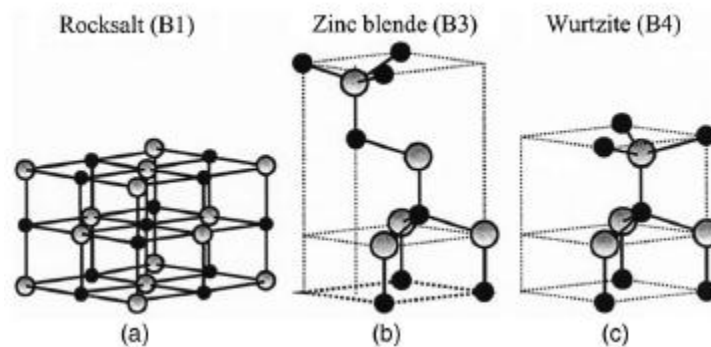


Figure 2 Stick and ball representation of ZnO crystal structures: (a)cubic rocksalt (B1), (b)cubic zinc blende (B3), and (c) hexagonal wurtzite (B4).The shaded gray and black spheres denote Zn and O atoms, respectively.

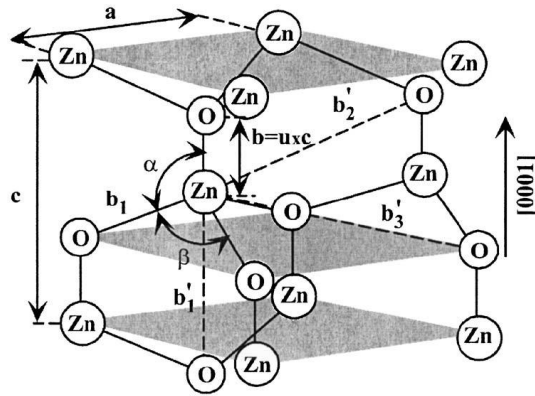


Figure 3 Schematic representation of a wurtzitic ZnO structure having lattice constants  $a$  in the basal plane and  $c$  in the basal direction;  $u$  parameter is expressed as the bond length or the nearest-neighbor distance  $b$  divided by  $c$  (0.375 in ideal crystal), and  $\alpha$  and  $\beta$  ( $109.47^\circ$  in ideal crystal) are the bond angles.

## 2.2 Cuprous Oxide (Cu<sub>2</sub>O)

Cuprous oxide (Cu<sub>2</sub>O), discovered at 1900's, is one of the oldest known semiconductors. It has attracted attention for solar cell applications as a typical p-type active layer.[24] In the literature there are many attempts to dope Cu<sub>2</sub>O *p*-type, but only nitrogen and chlorine gave clear results in decreasing the resistivity [25]. The former has been tested only on thin films and, due to the strength of the bond of the N<sub>2</sub> molecule, it is difficult to be inserted in bulk samples. Some studies have shown and suggested that the deposition of n-type Cu<sub>2</sub>O is also possible through controlling the intrinsic defects, i.e. the oxygen ion vacancies, in the Cu<sub>2</sub>O films.[26-29] However,

the origin of the n-type conductivity is still a matter of debate, with oxygen vacancies or copper anti-sites being suggested as the source of donors.[30]

The crystal structure of  $\text{Cu}_2\text{O}$  is cubic with a lattice constant of  $4.27\text{\AA}$ , the Cu–O bond length is  $1.85\text{\AA}$ , the O–O bond length is  $3.68\text{\AA}$  and the Cu–Cu bond length is  $3.02\text{\AA}$ . It has a direct band gap of  $2\text{eV}$  and high absorption coefficient. Among various metal oxide materials used for solar energy applications,  $\text{Cu}_2\text{O}$  is low-cost as its component elements are abundance and it is nontoxic. For photovoltaic applications, the highest conversion efficiency of the p–n heterojunction structure using  $\text{Cu}_2\text{O}$  as the active layer obtained so far was around 1% [31-34], while the Shockley-Queisser theoretical efficiency for  $\text{Cu}_2\text{O}$  based solar cells is about 13%.[35, 36] Therefore, there is still plenty of room for the scientists to improve its efficiency.

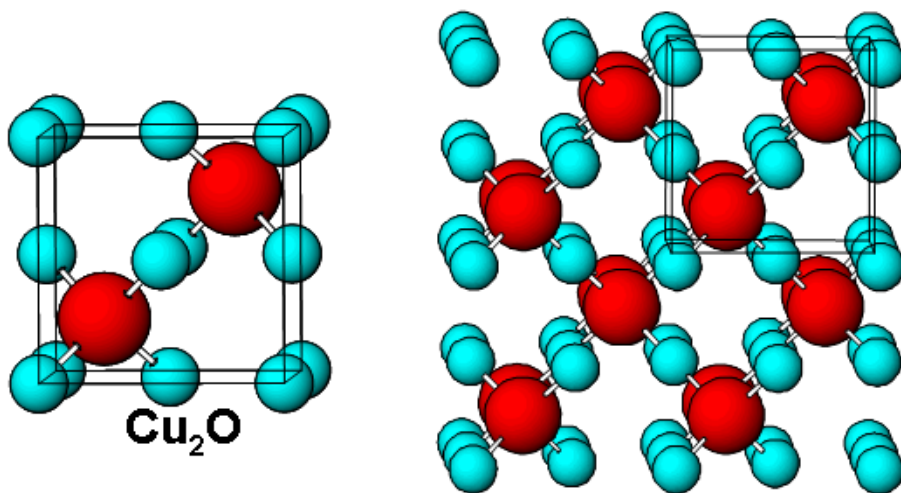


Figure 4 Drawings of the cuprous oxide ( $\text{Cu}_2\text{O}$ ) structure type emphasizing (left) the relation to antifluorite structure type and (right) the extended lattice demonstrating the diamond-like lattice connectivity. Copper atoms are drawn in blue and oxygen atoms in red.

## 2.3 Theories of Electrodeposition

In its simplest form, electrodeposition bath consists of an electrolyte, an electrode or substrate on which the deposition is desired, and a counter electrode. When a current flows through the electrolyte, the cations and anions move toward the cathode and anode, respectively, and films will be deposited on the electrodes after undergoing a charge transfer reaction. Historically, the discovery of electroplating is traced back to Michael Faraday and his famous laws of electrolysis: Faraday's First Law and Faraday's Second Law. The First Law states that the total amount of chemical change produced by an electric current is proportional to the total charge passing through the electrolyte. (Equation.2.1) The Second Law states that the masses of the different

substances liberated in the electrolysis are proportional to their chemical equivalent weights.

Expressed mathematically, the First Law relates the mass  $\Delta m$  deposited over a unit area to the current density  $j$  flowing for a time  $t$ :

$$\Delta m = C_e j t \quad (2.1)$$

Where  $C_e$  is the chemical equivalent constant. On the other hand, for the Second Law, an important implication is the introduction of Faraday constant ( $F$ ) which relates the molar mass of the electrodeposit ( $M$ ) with the chemical equivalent constant  $C_e$ . The Faraday constant is 96,500 colombs per mole. Therefore, the rate of growth of electrodeposit per unit area can be written as

$$\frac{d}{dt} \Delta m = C_e j = \frac{M}{zF} j \quad (2.2)$$

where  $z$  is the ionic charge. Thus, based on equations (2.1) and (2.2),  $\Delta m$  can be written as:

$$\Delta m = \frac{M}{zF} j \times t \quad (2.3)$$

The electrolyte or bath provides a medium for the suitable metal salts in the electrolyte to undergo electrodeposition. The electrolyte has to be electrically conductive. It can be either aqueous, nonaqueous, or molten. In the electrodeposition process, at least two electrodes (cathode and anode) are needed. An applied electric field across these electrodes provides the main "driving force" for the ions. In the simplest case, the positive ( $M^{Z+}$ ) and negative ( $X^{Z-}$ ) ions will be deposited at the cathode and anode, respectively. Cathodic deposition is more popular in electroplating because (1) most metal ions are positive ions and (2) anodic deposition has been found to give poor stoichiometry and adhesion[37].

Some common types of electrical driving forces that have been used for electroplating are shown in Figure 5. They are (1) direct current at constant voltage, which leads to potentiostatic deposition; (2) direct current at constant current, which leads to galvanostatic deposition; or (3) a current or voltage waveform or pulse as shown in Figures 5(b)– 5(e) .

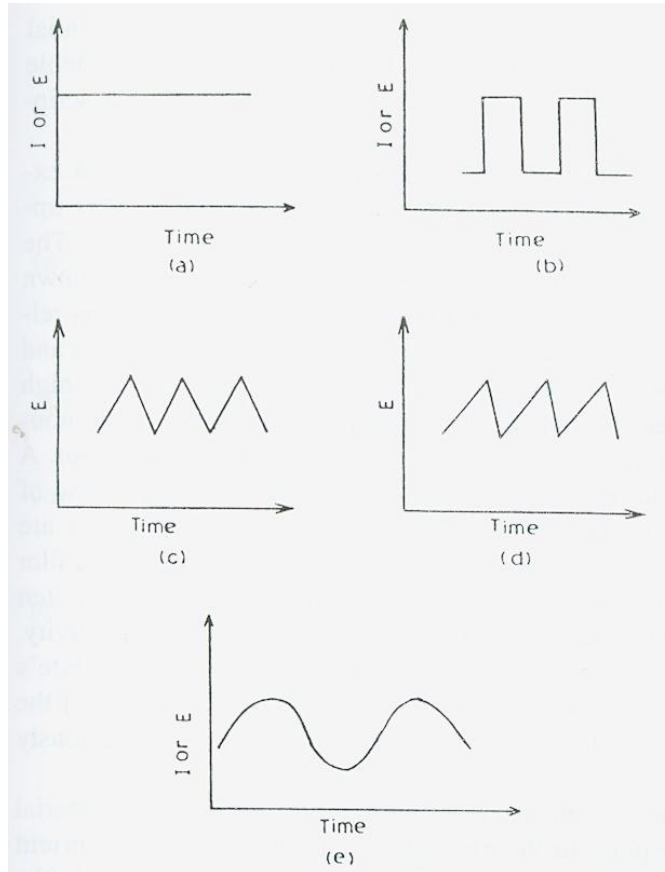


Figure 5 Types of electrical driving forces (current or potential). (a) Direct current source; (b) a square wave or pulse; (c) :1 triangular wave; (d) a cyclic ramp; (e) a sinusoidal wave.

Consider a cathodic electrodeposition reaction involving  $M^{z+}$  ions. The ion is either in forms of hydrated ( $M^{z+} \cdot nH_2O$ ) or in complex (with any ligand or solvent,  $MA_x^{z-x}$ ) form.

In general, the above electrodeposition occur in four successive steps: 1) ionic transport, 2) discharge, 3) breaking up of ion—ligand bond (sometimes this step is skipped), 4) incorporation of adatoms onto the substrate followed by nucleation and growth.

These four steps occur within 1-1000 Å from the substrate. However, each has its own region of operation, as shown in Figure 6. The various processes can be classified into processes that occur (1) in the electrolyte bulk, (2) near the electrode, and (3) at the electrode.

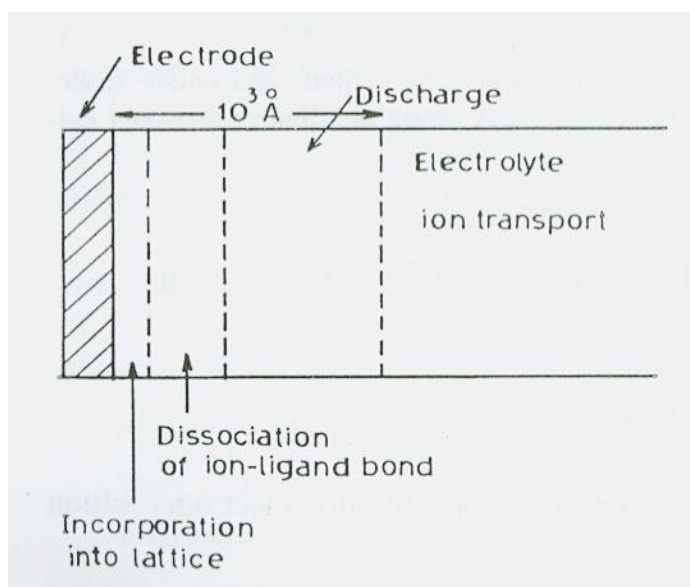


Figure 6 Approximate regions in which various stages of ion transport occur leading to electrodeposition,

In a practical cathodic electrodeposition, the interfacial potential drop with respect to a reference electrode at the cathode is replaced by the reference equilibrium electrode potential  $E_e$ , and the Nernst equation (Equation 2.4) can be written as:

$$E_e = E_e^0 + \frac{RT}{zF} \ln \frac{a_{M^{z+}}}{a_M} \quad (2.4)$$

where  $E_e^0$  is the standard equilibrium electrode potential (with respect to a reference

electrode) when activities  $a_{M^{z+}}$  and  $a_M$  in the electrolyte and the deposit, respectively are equal. In this case,  $E_e$  is also equivalent to the reversible electrode potential corresponding to  $a_{M^{z+}}$  and  $a_M$ . Here  $R$  is the universal gas constant and  $T$  is the temperature.

However, truly reversible electrode potentials are rarely met in practice due to the following reasons: 1) the processes leading to the electrodeposition of  $M$  are fast compared to other competing reactions, 2) the bath contains an equilibrium concentration of the soluble species, 3) the electrodeposit is in a pure and well-defined phase, and 4) the crystallite sizes are not too small, they should be greater than 25 nm.

Knowledge of these thermodynamic data i.e. standard equilibrium electrode potential and the reversible electrode potential, is useful in assessing the ability to deposit a particular species. For example, if the electrode potential under the application of an external field is  $E$  when a current  $j$  is flowing, then the overpotential departs from its equilibrium value  $\eta_a$  can be expressed as:

$$\eta_a = E - E_e + jR_e$$

where  $jR_e$  is the ohmic drop.

The current  $j$  can be further expressed using Butler—Volmer equation:

$$j = j_0 \left[ \exp\left(\frac{zF_{\alpha_c} \eta_a}{RT}\right) - \exp\left(\frac{zF_{\alpha_a} \eta_a}{RT}\right) \right] \quad (2.5)$$

where  $F_{\alpha_c}$  and  $F_{\alpha_a}$  is the Faraday constant,  $\alpha_c$  and  $\alpha_a$  is the transfer coefficient of the cathodic and anodic charge transfer reaction, respectively.

Based on the Butler—Volmer equation (Equation 2.5) and Nernst equation (Equation 2.4), one can draw an important conclusion using purely thermodynamic arguments.

The electrodeposition of an ionic species  $M^{z+}$  can occur only at potentials that are more negative than its standard equilibrium potential  $E_e^0$ .

Besides the theoretical calculations, a linear voltammetry technique offers another way to assess the deposition potential in practical (details in section 2.4). Since the potential to be employed is not always known beforehand, ramping the cell potential in the region without solvent electrolysis, that is the potential of hydrogen evolution and oxygen evolution for aqueous solution. Nevertheless, one or more of synthetic parameters may have to be empirically selected by performing a large number of trials, keeping in view the product quality.

## 2.4 Cyclic voltammetry

Cyclic voltammetry is the most widely used technique in electrochemistry. It acquires qualitative information about electrochemical reactions occurring on the electrode surface.

From the results of cyclic voltammetry, it is able to rapidly obtain considerable information on a) the thermodynamics of redox processes, b) the kinetic of heterogeneous electron-transfer reaction, and c) the coupled chemical reaction or adsorption processes.

In a typical cyclic voltammetry, chemicals in electrolyte are oxidized or reduced on the immersed electrode surface by imposing sufficiently positive or negative potential on it to force electron transfer. Normally, the potential is in a triangle waveform. In simple case, the cathode electrode (working electrode) surface is started at a particular potential with respect to a reference. The electrode potential is then swept to a higher or lower value at a linear rate, and finally, the potential will sweep back to the original value at the same linear rate (Figure 7).

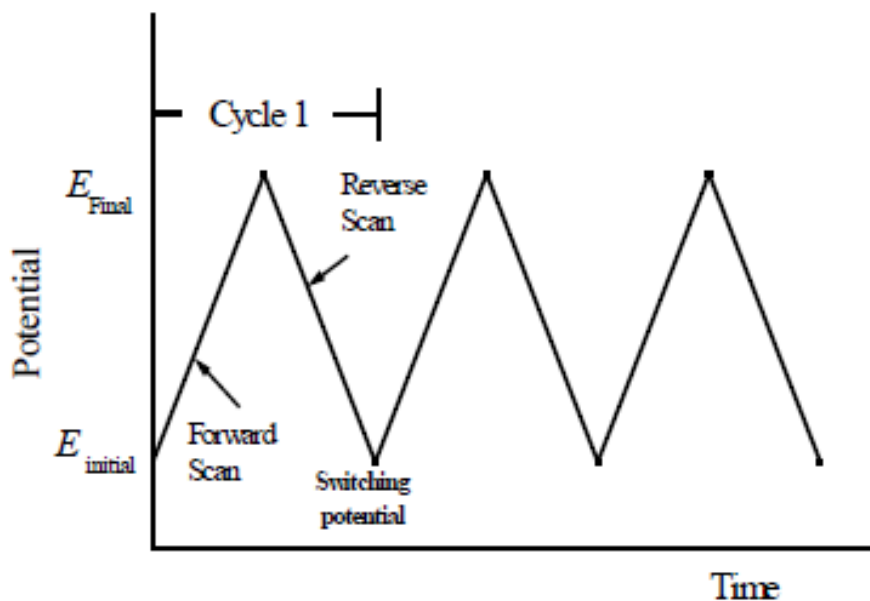


Figure 7 Potential-time signal in cyclic voltammetry experiments[38].

General speaking, the electrochemical reaction of interest takes place at the working electrode (WE). The process at counter electrode is typically not of interest, and in most experiments the small currents observed at counter electrode mean that the electrolytic products at counter electrode have no influence on the processes occurred at the WE.

Electrode potential of single or multiple cycles can be applied depending on the information sought. During potential sweep, the potentiostat measures the faradaic current at the WE. The resulting plot of current versus potential is called cyclic voltammogram, which is a complicated and time-dependent function of a large number of physical and chemical parameters.

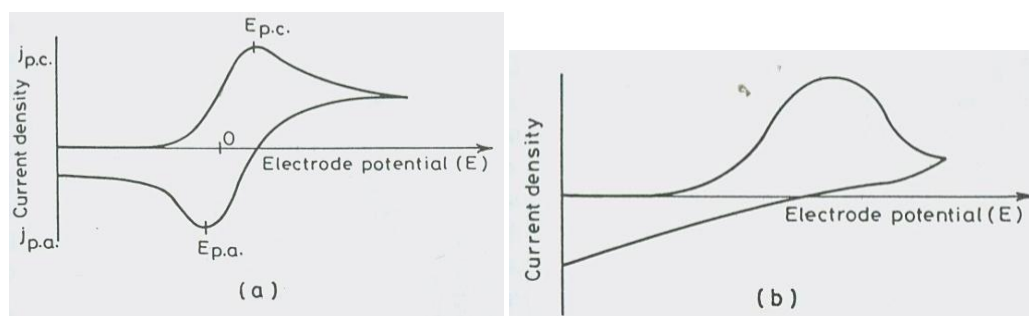


Figure 8 Typical cyclic voltammogram for a) a reversible  $O + ne \rightleftharpoons R$  redox processes and b) irreversible processes.  $E_{p.c.}$  and  $E_{p.a.}$  represents the cathodic peak and anodic peak current, respectively [37].

Typical voltammograms obtained for reversible and irreversible systems are schematically shown in Figure 8. The scan begins at a value where no reduction occurs and to sweep towards negative potential for the first half-cycle. Then, a cathodic current begins to increase, until a peak is reached. After traversing the potential region where the reduction process takes place, the direction of the potential sweep is reversed. During the reverse scan reduced molecules are oxidized and an anodic peak results. In comparison, the reversible voltammograms are marked by current peaks in the cathodic and anodic sweep directions, while the irreversible process is generally characterized by the absence of the peak in the anodic sweep. In addition, there are no peak in the reversed sweeping process for semiconductors.

Cyclic voltammetry has been proved to be a very popular and useful probe, particularly

when one is studying a new system. The cyclic voltammogram is characterized by several important observable parameters, including the two peak currents and two peak potentials. They provide the basis for the diagnostics in order to analyze the cyclic voltammetric response.

## 2.5 Mott-Schottky Plot

In order to determine the parameters such as carrier density, flatband potential and conduction type of the semiconducting materials, there is a method measuring the apparent capacitance as a function of potential under depletion condition and follow on the Mott-Schottky relationship:

$$\frac{1}{C_{sc}^2} = \frac{2}{e\epsilon\epsilon_0 N} \left( E - E_{FB} - \frac{kT}{e} \right) \quad (2.6)$$

where:

$C_{sc}$  = capacitance of the spacecharge region

$\epsilon$  = dielectric constant of the semiconductor

$\epsilon_0$  = permittivity of free space

$N$  = charge carrier density (electron donor concentration for an  $n$ -type semiconductor or hole acceptor concentration for  $p$ -type semiconductor)

$E$  = applied potential

$E_{FB}$  = flatband potential

A negative slope and a positive slope of Mott-Schottky plots ( $1/C^2$  vs.  $E$ ) represent for a

*p*-type and an *n*-type semiconductor, respectively. Furthermore, the donor density can be calculated from the slope, and the flatband potential can be determined by extrapolation to  $1/C^2 = 0$ . The capacitance values are calculated from impedance measurements. Basically, this C – V measurements are performed by applying a dc bias in order to widen or shrink the depletion layer and a small superimposed ac signal voltage for probing the actual capacitance at a given bias. Often the junction capacitance shows a dependence on the measurement frequency. When a given frequency is selected, the imaginary component of the impedance can be calculated at this frequency for each potential.

There are two assumptions for the calculation based on this model[39]:

- 1) There are two capacitances to be considered during the measurements, namely the capacitance arisen from the space charge region as well as the capacitance of the double layer. In general, the space charge capacitance is much smaller than the double layer capacitance (2-3 orders of magnitude). Since these two capacitances are in series, the total capacitance is the sum of their reciprocals. The contribution of the double layer capacitance to the total capacitance will be negligible. Therefore, the capacitance value calculated from this model is assumed to be the value of the space charge capacitance.
- 2) The frequency is high enough (on the order of kHz). The equivalent circuit used in

this model is a series combination of a resistor and a capacitor (the space charge capacitance). The capacitance is calculated from the imaginary component of the impedance ( $Z''$ ) using the relationship  $Z'' = 1/2\pi fC$  where  $f$  is the frequency. High frequency helps to keep the behavior of the circuit equivalent to a capacitor and a resistor in series.

More detailed model of the junction includes trap levels in the band gap or at the interface and surface states whose charging and discharging adds to the depletion layer capacitance which explains the observed frequency dependence. Also considering the effects of polar groups and  $\epsilon_s$  variation, it may be remarked here that the Mott- Schottky plots are not found to be linear.

## **2.6 Photoelectrochemical measurement**

Photoelectrochemical (PEC) measurements give information about conduction type of the film after deposition. The measurements are performed in an electrolyte solution that contains a redox species. The redox potential is at a suitable position with respect to the band edges of the semiconductor so that charge-transfer reactions between the semiconductor and the solution are possible. [39]

When a semiconductor is immersed in the electrolyte, an electric field will be developed at the solid/liquid interface via charge transfer reactions between the two phases. The electric field enables the separation of charge carriers, analogously to a pn-junction or a Schottky junction. Illumination of the semiconductor causes a dramatic increase of the concentration of minority carriers, for example electrons in a p-type semiconductor. The electric field drives the photo generated minority carriers towards the semiconductor/liquid interface, where they may participate in the electrochemical reactions occurred in the solution with a suitable redox species. Thus a p-type semiconductor is capable of reducing more species under illumination than in the dark, causing an increase of cathodic current while the anodic current remains unaffected. An n-type semiconductor acts in the other way: anodic current is enhanced under illumination as compared to dark, whereas cathodic current is not affected. Semiconductor/liquid junctions are the basis of photoelectrochemical solar cells that are used for production of electricity or fuels. The photoelectrochemical properties of semiconductor electrodes has been studied a lot [39].

In addition to conductivity type, PEC measurements can also be used for the determination of flat-band potential. However, the band edge positions of photoactive deposit are strongly dependent on the electrolyte and on the surface chemistry of the

film which may complicate the interpretation of the data [40].

## **2.7 X-Ray Diffraction**

It is important to determine the crystal structure of the deposited film in order to reveal the correlation between structural properties and electrical as well as optical properties. General speaking, amorphous semiconductors have advantages of uniform and ease of deposition at room temperature, while crystalline structures usually have better electrical performance than amorphous structures. Therefore, it is important to XRD technique to investigate the structural properties such as lattice parameter and grain size of the films.

X-ray is an electromagnetic wave with wavelength in the range of 0.001 to 10 nm. It is produced when high-energy electron beam is directed into a water-cooled target to generate X-rays. Most of the electron beam energy loses in the collision with the target that decelerates the atoms in motion. This collision produces heat which must be dissipated through the cooling water. The decelerated electron caught in the electric fields of the atom produces X-rays of a continuum of all energies between zero and the excitation potential, and is termed as white or bremsstrahlung radiation. Some target electrons are knocked out of their orbitals, for which these electron transitions are

quantified and have specific wavelengths. Therefore, X-rays have a few strong characteristic concentrations of specific wavelength superimposed on the white radiation. Copper is usually used as the target because the  $K_{\alpha}$  characteristic radiation has a useful wavelength of 0.15406nm, and the Cu target is easily cooled with high efficiency. A nickel foil is always used as a filter to absorb most of the white radiation and transmit essentially pure  $K_{\alpha}$  radiation. A detector filled with Xe gas is used as it is particularly good for detecting radiation emitted from Cu.

When X-rays are incident on a sample, the electrons in the sample atom interact with X-rays and electromagnetic radiation is emitted again. This process is called scattering. The overlapping of two or more scattered waves produces a resultant wave that is a sum of various amplitudes at each point. A constructive interference of more than one scattered wave is called diffraction.

Normally the scattered X-rays are out of phase and cancel each other. However, at certain distances between the atom planes in the sample, the scattered X-rays will be in phase. This relationship follows the Bragg's law:

$$n\lambda = 2d \sin\theta \quad (2.7)$$

Where n is an integer,  $\lambda$  is the wavelength of the incident X-rays,  $\theta$  is the deflection

angle and  $d$  is the distance between the atom planes. When Bragg's law is fulfilled, the X-rays leaving the sample are in phase and the beam is diffracted.

In a diffraction pattern, the recorded intensity is plotted against the deflection angle,  $2\theta$ . Each peak in the diffractogram can be correlated to a crystal planes separation. The width of the peak provides the information about the crystal size. Broadening of the peaks represents small crystals and vice versa.

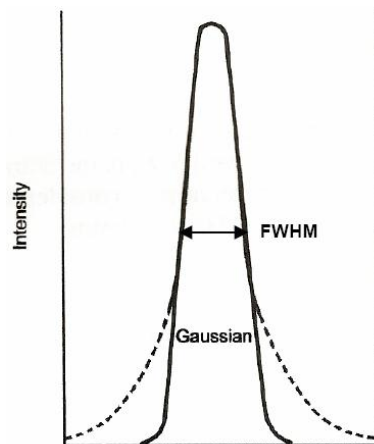


Figure 9 Gaussian x-ray diffraction peak profile.

Crystallite size is determined using the Scherrer equation:

$$L = \frac{k\lambda}{B_r \cos \theta} \quad (2.8)$$

Where  $\lambda$  is the wavelength of the X-rays used,  $B_r$  is the width of observed X-ray peak,  $\theta$  is the Bragg angle,  $L$  is the average crystallite size measured in a direction perpendicular to the surface of the specimen, and  $k$  is a constant, with the assumption

that  $k = 0.9$ . However, this equation is suitable for grain size smaller than 100nm only.

## **2.8 Scanning Electron Microscopy**

Scanning electron microscopy offers the morphological and topographical information of the solid surfaces that are necessary in understanding the behavior of the surfaces.

The sample in SEM chamber is bombarded with an electron beam. In comparison with optical microscopy, SEM uses electrons with a shorter wavelength compared with visible light and thus creates a better resolution. Therefore, it has ability to generate higher magnification pictures from the sample surface.

In an SEM instrument, the electron beam, which is emitted from the filament in the electron gun, is accelerated towards the sample and focused by several condenser lenses. Since the sample acts like an anode for the probing electron beam, the sample should be conductive to avoid accumulation of charges. If a non-conductive sample is characterized, a thin layer of gold will usually be sputtered on the surface of the sample to pass the current. When the focused beam hits a point on the sample, numerous collisions between the electrons from the beam and atoms in the sample will occur. The outer most electrons of the atoms in the sample will be detached due to these collisions.

These electrons have relatively low kinetic energy and can easily be attracted by the detector. The electrons generated from this process are called secondary electrons.

The detector counts the number of electrons emitted from this small area and records the origination from each point. The result is displayed as point on a computer screen. A magnified image of the sample is created by scanning the electron beam over a smaller area. Both the topography and the atom numbers of the sample affect the number of secondary electrons emitted. The resulting image has shadows and perspective, just like ordinary photographs. According to those factors, the SEM micrographs are consequently easy to interpret.

## **2.9 Electrical measurement**

Resistivity is one of the most important electrical parameters of semiconductors. From a macroscopic point of view, the resistivity  $\rho$  can be viewed as the normalization of the bulk resistance ( $R$ ) by its geometrical dimensions (i.e., the cross-section area,  $A = Wt$ ). The bulk resistivity  $\rho$  is an intrinsic electrical property related to carrier drift in materials such as metal and semiconductors [41]—the cross-sectional area ( $A = Wt$  where  $w$  is the width and  $t$  is the thickness.) through which the current flow, and the distance between the two ideal contacts  $L$ , as shown in Fig. 10. The resistivity is given

by

$$\rho = \frac{RA}{L} \text{ in } \Omega\text{-cm} \quad (2.9)$$

For thin semiconductor layers, the sheet resistivity  $\rho_s$  is often used instead of the bulk resistivity  $\rho$ . The sheet resistivity  $\rho_s$  ( $\rho_s = \rho / t$ ) is the bulk resistivity divided by the sample's thickness,  $t$ . This normalized parameter is related to the resistance of a square of side  $L$ . For this particular geometry in Figure 10, since  $A = Wt$  and  $W=L$ , then  $\rho_s = R_{\square}$ , the sheet resistance. The unit of sheet resistance is  $\Omega/\text{square}$  or  $\Omega/\square$ . The parameter  $R_{\square}$  is convenient for integrated circuit designers because it allows them to quickly design the geometry for a specific value of resistance using very thin implanted or diffused semiconductor regions or polycrystalline layers. Resistivity (or its inverse, the conductivity  $\sigma$  in  $\Omega^{-1}\text{cm}^{-1}$  or  $\text{S/cm}$ ) and its variation with temperature is often used to classify materials into metals, semiconductors and insulators.

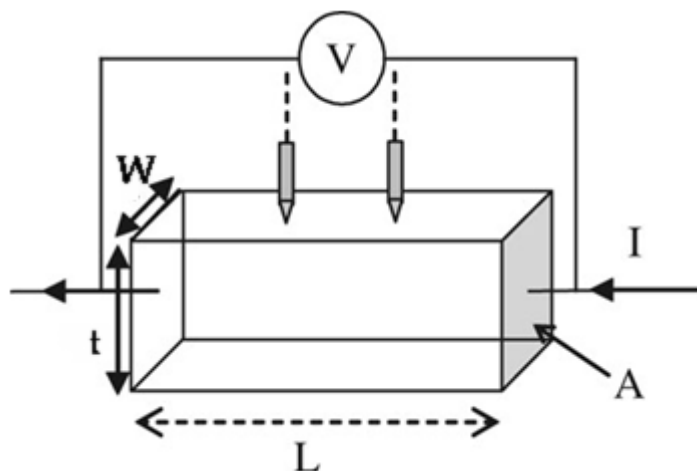


Figure 10 Bulk resistance and its geometrical dimensions

For a given semiconductor, different values of resistivity can be found because it depends on the fabrication process. Moreover, resistivity is not a fundamental material parameter since it can be further explained by solid-state theory. In the case of a homogeneous semiconductor material, the resistivity is proportional between the applied electric field  $E$  and the drift current density  $J$ , that is,  $J = \left(\frac{1}{\rho}\right) E$ . It can be defined by the microscopic relation:

$$\rho = \frac{1}{q(n\mu_n + p\mu_p)} \quad (2.10)$$

where  $q$  is the electronic charge,  $n$  and  $p$  are the free electron and hole concentrations, and  $\mu_n$  and  $\mu_p$  are the electron and hole drift mobilities, respectively. According to Equation (2.10), the resistivity is related to fundamental semiconductor parameters, namely, the number of free carriers and their ability to move in the lattice under the influence of an applied field.

In n-type (donor,  $N_D$ ) or p-type (acceptor,  $N_A$ ) doped semiconductors, assuming  $N_D$  or  $N_A \gg$  intrinsic carrier concentration  $n_i$ . The free carrier densities are determined by the ionized impurities. Then Eq. 2.9 can be simplified [42] to:

$$\rho \approx \frac{1}{qn\mu_n} , \text{ for n-type semiconductor} \quad (2.11a)$$

$$\rho \approx \frac{1}{qp\mu_p} , \text{ for p-type semiconductor} \quad (2.11b)$$

The measurement of resistivity is not straightforward for the electrodeposited semiconductors because the electrodeposited films are necessarily on a metallic or conducting substrate. Therefore, reports on resistivity measurements on electrodeposited films are scanty, and the reports that exist in the literature must be read with caution. The following two situations may arise.

1. The metal substrate forms a low-resistance ohmic junction with the semiconductor electrodeposited films. In such a case, two-electrode sandwich arrangement with metal/semiconductor/metal symmetric geometry gives reasonable results. To test this, the current-voltage characteristics in both forward and backward bias are plotted and a symmetric plot should be resulted (Fig. 11). From the slope of the current-voltage plots, the resistivity  $\rho$  can be calculated as

$$\rho = \frac{\partial V}{\partial i} \left( \frac{A}{t_f} \right) \quad (2.12)$$

where A is the area of electrode and  $t_f$  is the thickness of the film.

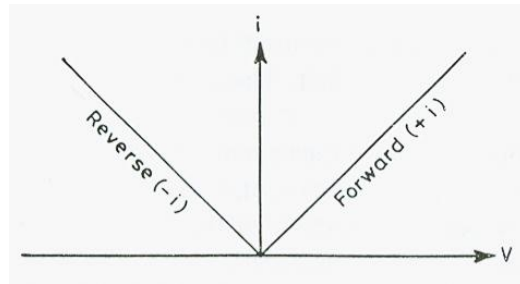


Figure 11 A typical symmetric current-voltage (i-v) characteristic of a metal-semiconductor-metal structure.

2. The metal forms a nonohmic contact (i.e., the i-V curve is nonsymmetric) or the contact resistance is high. In this case the two-electrode method fails. This is the most common situation. There are two possible solutions, each with its own limitations: a) All or part of the film is lifted by using an “adhesive tape” technique. The resistivity measurements are then done using the four-probe (Van der Pauw) technique discussed below. This has a serious limitation if the electrodeposited film has a good adhesion with the substrate. In this case large force will be needed to lift the film, which may result in the film being stressed.

b) If the substrate sheet resistivity is order of magnitude higher than the resistivity of the semiconductor electrodeposited film, one can approximate the substrate as insulating and follow the Van der Pauw technique. The limitations of this method are quite obvious because it is hardly possible to get good large-area electrodeposited films on substrates with high sheet resistivity.

## 2.10 Schottky contact

A Schottky contact is a junction that between a metal and a semiconductor. The formation of Schottky contact is shown in Figure 12. Black dots in the graph represent electrons. When metal and semiconductor are separated from each other, their Fermi levels ( $E_F$ ) are different in energy (Figure 12a). At the moment they contact with each other, their  $E_F$  are still remain different as they separated at infinity without thermodynamically equilibrium (Figure 12b). In order to achieve the equilibrium, electrons move into the metal from the semiconductor as the arrows shown. Electrons find lower energy states, which are also empty, with a large density of states of metals.

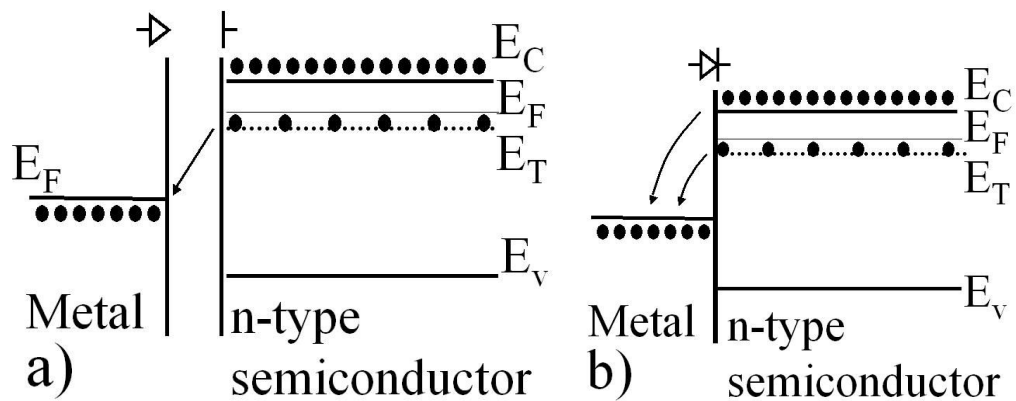


Figure 12 Formation of a Schottky contact. a) Situation if there is no contact between the metal and the n-type semiconductor. b) Hypothetical situation if the materials would be brought suddenly into contact. No surface states that might pin the  $E_F$  are assumed. For clarity, any possible hole concentration is neglected.

The number of electrons close to the metal contact deplete, therefore, cause band bending in the semiconductor. When thermodynamic equilibrium is achieved, both  $E_F$  of the semiconductor and the metal are aligned at the same level and a depletion of thickness  $d_0$  region is formed, containing positive ions  $N_{ion}$  (open circles with a plus sign inside), as shown in Figure 13.

Assuming there are no free carriers in the depletion region (this is known as the depletion approximation), a layer of electrons is formed on the metal side. The position of the layer of positive ions and of electrons should not be regarded as a function of energy. They are drawn just for descriptive purposes.

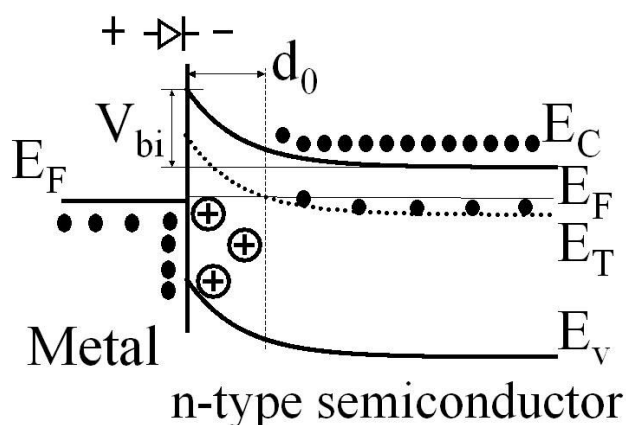


Figure 13 Schottky contact in thermal equilibrium. There is a layer of electrons in the metal side, and a layer of positive ions in the n-type material. The depletion region in the n-type material has a thickness  $d_0$ .

The current through a Schottky diode is expressed by the thermionic emission-diffusion equation(2.13) :

$$I = I_s(e^{qV/nkT} - 1) \quad (2.13)$$

where  $I_s$  is the saturated diffusion current,  $q$  is the charge of the electron,  $V$  is the voltage across the Schottky diode according to the polarization shown in Figure 13,  $k$  the Boltzmann constant,  $T$  the absolute temperature and  $n$  the ideality factor.  $I_s$  is a temperature dependent variable, and depends on  $V_{bi}$  according to

$$I_s = A^{**}T e^{-qV_{bi}/kT} \quad (2.14)$$

where  $A^{**}$  is the Richardson constant, a parameter depending on the effective mass of the carriers. Usually, one plots and linearly fits the natural logarithm of  $I$  versus  $V$  of Equation 2.13. The constant term yields  $I_s$ , and the slope  $n$  lies between 1 and 2. The closer the value to one, the more the transport process is caused by the thermionic emission. When the value is close to two, diffusion is the governing transport mechanism. Values out of this range are usually attributed to low crystal quality, such as an interfacial layer or surface states existing between the semiconductor and the metal.

## 2.11 Ultraviolet-Visible spectroscopy

The ultraviolet-visible (UV-Vis) spectroscopy is important in the optical characterization of semiconductor. It aims to measure the band gap of materials. The determination of bandgap ( $E_g$ ) energy can be used to distinguish insulator and semiconductor as the former one has large  $E_g$  ( $> 4\text{eV}$ ), but latter one has low  $E_g$  ( $< 3\text{eV}$ ). Moreover, the band gap energy of a semiconductor can be controlled by doping impurities such as indium, magnesium, aluminum, gallium into semiconductor. Being a solar cell, the bandgap energy is important as it determines the portion of the solar spectrum that a photovoltaic cell absorbs. Photons with energies larger than  $E_g$  will be absorbed by the solar cell, and the excess energy is converted into heat rather than usable electrical energy. Consequently, the band gap energy must be optimized in order to enhance the efficiency of the solar cell. Therefore, UV-Vis spectroscopy is commonly used to monitor the effects of dopants on the bandgap energy.

Band gap energy ( $E_g$ ) refers to the quantized energy difference between the top of the valence band to the bottom of the conduction band (Figure 14). Electrons are able to jump from one band to another when a specific amount of energy larger than  $E_g$  for the transition is provided.

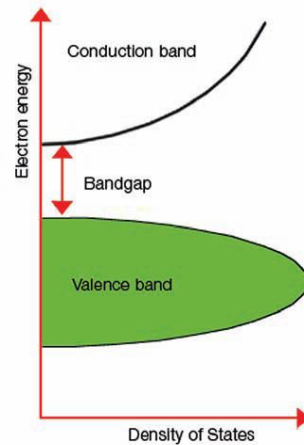


Figure14 Schematic diagram of the band structure of semiconductors.

The band gap energy of the semiconductor deposited on opaque substrates are usually measured by diffuse reflectance spectroscopy. This method is not affected by temperature and surface defects.

As diffuse reflectance spectroscopy actually entails both specular and diffuse reflectance, the Kubelka-Munk function is used to convert absorbance to a function of reflectance.

Specular reflection occurs when the sample reflects, but does not absorb, incident light radiation. Diffuse reflection occurs when the sample absorbs light before reflecting it.

Simply put, the Kubelka-Munk function determines the ratio of the coefficients for absorbed to scattered light. For an optically thick sample, the Kubelka-Munk function is defined as follows:

$$f(R_{\infty}) = \frac{\alpha}{S} = \frac{(1-R_{\infty})^2}{2R_{\infty}} \quad (2.15)$$

where  $\alpha$  and  $S$  are the effective absorption coefficient and scattering coefficient per unit thickness of the film, respectively, and  $R_{\infty}$  is the total diffuse reflectance from the thick sample and the relationship with thin film reflectance  $R_{\text{Film}}$  is  $R_{\infty} = R_{\text{Film}}/R_{\text{Substrate}}$ , where  $R_{\text{Substrate}}$  is the reference reflectance

For practical UV-Vis experiments, absorbance ( $A$ ) is converted to transmittance ( $T$ ) using Equation (2.16).

$$A = -\log(T) \quad (2.16)$$

Transmittance is actually reflectance for solid samples in our UV-Vis setup, so reflectance values were used to determine  $f(R_{\infty})$  for each sample. Note that transmittance is often given in percent values, but here it is in decimal form. When  $f(R_{\infty})$  is plotted versus energy, extrapolating the onset of increasing  $f(R_{\infty})$  to the energy axis gives the band gap energy [43]. Band gap energies presented in this chapter and Chapter 4 are found based upon this method.

$$(h\nu \propto)^n = C(h\nu - E_g) \quad (2.17)$$

where  $n$  is 2 for direct gap material or  $1/2$  for indirect gap material.

## **2.12 Photoluminescence spectroscopy**

Photoluminescence belongs to the luminescence spectroscopy, which is a powerful tool used for the characterization of semiconductors in optoelectronic devices. The utilization of this nondestructive characterization technique is benefit from its sensitive to the bandgap, impurities and defects that affect materials quality and device performance.

In general, luminescence is used to describe the process of light emission after some forms of energy are interacted with the material through an excitation source. There are several ways to excite sample to cause luminescence. For photoluminescence, the excitation source is photon. We can briefly say photoluminescence process includes three main phases [24]:

- 1) Excitation: Electrons absorb energy from external light sources, such as lasers, arc-discharge lamps, and tungsten-halogen bulbs. After absorbing energy, the electrons are promoted to higher energy levels. In this process electron-hole pairs are usually created.
- 2) Thermalization: The excited pairs relax towards quasi-thermal equilibrium distributions.

3) Recombination: The energy is subsequently released, in the form of lower energy photon, when the electrons fall back to the original ground state. This process can be occurred radiatively or non-radiatively. For radiative decay, relaxation results in the production of photons that are characteristics of the crystal or defect site.

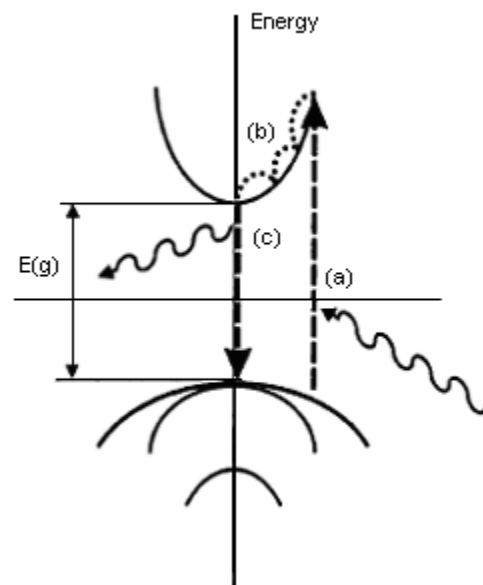


Figure 15 Photoluminescence schematic. (a) An electron absorbs a photon and is promoted from the valence band to the conduction band. A electron-hole pair is generated (b) The electron cools down to the bottom of the conduction band. (c) The electron recombines with the hole resulting in the emission of light with energy  $h\nu$ .

The luminescent signals might be the results from band to band recombination, intrinsic crystalline defects (growth defects), dopant impurities (introduced during growth or ion implantation), or other extrinsic defect levels (as a result of radiation or thermal effects)

via several different types of radiative recombination events. Therefore, the PL spectra are commonly used to determine the specific type of defect in semiconductors.

For photoluminescence with life time less than about 1  $\mu\text{s}$  after excitation, it is commonly called fluorescence. For emission happens after 1  $\mu\text{s}$  or lasts long times (up to hours and days), it is called phosphorescence.

Other possible ways can be used to excite the sample, for example, external electrical current, external heat, energy-rich electrons, and energy from chemical reactions. Under these circumstances, they are called electroluminescence, thermoluminescence, cathodoluminescence and chemoluminescence, respectively. However, they are not the scope of this thesis and are not discussed here.

## Chapter 3 Experimental section

### 3.1 Substrates preparation

Copper coated polyethylene terephthalate (Cu/PET) sheet were employed as substrates in our experiments. The metallization process of PET sheet followed the standard procedures which had been previously reported by our group [8]. Prior to the film deposition, the substrates were cleaned with absolute acetone, 0.5M HCl and finally with absolute acetone again for 1 minute, 5 minutes and 1minute.

### 3.2 Electrodeposition of metal oxide

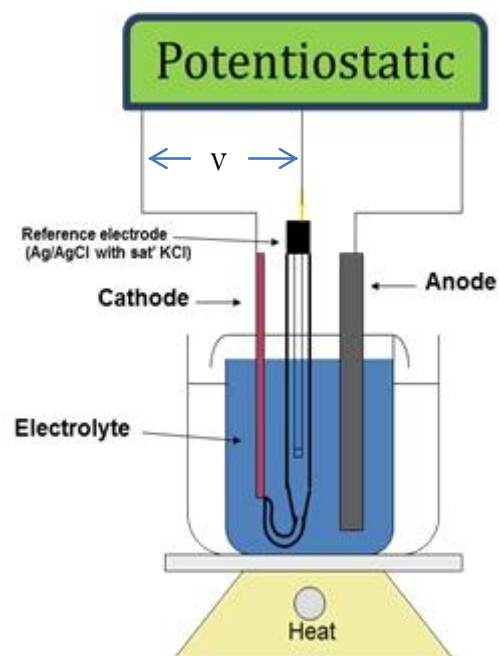


Figure 16 The schematic setup for electrodeposition experiment. All the mentioned voltages in voltage scanning and electrodeposition are the results of cathode versus the reference electrode (Ag/AgCl with saturated KCl) but not anode.

A three electrode system (Figure 16) was used to perform all electrochemical cell process. The electroplating system was composed by a Ag/AgCl (saturated KCl) reference electrode (RE) and a graphite counter electrode (CE). The Cu/PET substrates located at cathode were used as working electrodes (WE). An EG&G PAR 2273 potentiostat was used to perform and monitor the deposition process. The cyclic voltammetry measurements were carried out using the same instrument to analyze the reactions on WE. All voltages, which related to the electrochemical process, mentioned in this thesis were taken against Ag/AgCl (saturated KCl) reference electrode without further specifications.

### **3.2.1 Zinc Oxide**

To synthesis ZnO films, zinc nitrate hexahydrate powder was dissolved in deionized water to make electroplating baths of aqueous zinc nitrate solution with pH value of 3.6. The cyclic voltammetry measurement was carried out at a scan rate of 20mV/s with scanning potential ranging between +0.2V and -1.5V, according to our preliminary test results and reference from other group [44]. Seven sets of samples (Table 2) with various deposition potential, bath concentration and deposition temperature were fabricated. All the samples had the same deposition time of 16 minutes.

Table 2. Electrodeposition conditions of ZnO samples on Cu coated PET from zinc

nitrate bath.

Sample no.	Deposition potential [mV versus Ag/AgCl]	Bathconcentration [M]	Temperature [°C]
A	-400	0.01	80
B	-550	0.01	80
C	-700	0.01	80
D	-550	0.1	80
E	-550	0.5	80
F	-550	0.1	60
G	-550	0.1	40

### 3.2.2 Cuprous Oxide

The details of deposition have been discussed elsewhere [1, [24, 36]. A total 45 g of cupric sulphate pentahydrate was dissolved in 75 ml of 88% lactic acid and then 225 ml of a 5M NaOH aqueous solution was added to make the pH of the solution to 10. As a result, 3.25 M lactic acid and 0.45 M cupric sulphate were mixed to form the copper lactate solution, which was act as an electrolyte. The cyclic voltammetry measurement was carried out before the potentiostatic deposition. Both the cyclic voltammetry measurement and electrodeposition were carried out at a bath temperature of 40°C. A scan rate of 20mV/s was used to sweep from +0.1V to -1.0V and then backward. The selected range was based on preliminary test results and studies from other groups [45], [46]. Six sets of samples (Table 3) with various deposition potentials and deposition times were fabricated.

Table 3. Electrodeposition conditions of Cu<sub>2</sub>O samples on Cu coated PET from copper(II) lactate bath.

Sample no.	Deposition potential [V versus Ag/AgCl]	Time [mins]
1	-0.15	30
2	-0.30	30
3	-0.45	30
4	-0.50	30
5	-0.60	30
6	-0.70	30
7	-0.45	15
8	-0.45	45
9	-0.45	60

### 3.2.3 Hetero-junction of Zinc Oxide/Cuprous Oxide



Figure 17 The schematic structure of the layer-by-layer ZnO/Cu<sub>2</sub>O heterojunction .

The schematic structure of the ZnO/Cu<sub>2</sub>O heterojunction was shown in Figure 17. After using the above mentioned method to deposit a Cu<sub>2</sub>O layer onto the Cu-coated PET substrate using the optimal one, a layer of ZnO was further electrodeposited on it by using the optimized conditions. The cyclic voltammetry measurement was carried out at a scan rate of 20mV/s with a range between +0.5V and -1.5V based on preliminary test results. A 0.1M aqueous zinc nitrate solution with pH value of 3.6 was

employed as the electroplating baths with a potential of -0.55V.

### **3.3 Photoelectrochemical studies**

Photoelectrochemical studies were conducted in a three-electrode electrochemical cell (the setup of Fig. 16) containing 0.1 M sodium hydrocarbonate as the electrolyte. The EG&G PAR 2273 potentiostat was used to record the current response from the sample. A halogen lamp was switched on and off manually to stimulate the oxide layer on working electrode.

### **3.4 Mott-Schottky plot**

The Mott–Schottky measurements were performed in a three-electrode cell using EG&G PAR 2273 potentiostat. A carbonate propylene electrolyte, which contained 0.1 M  $\text{LiClO}_4$ , was used to avoid decomposition of the as-grown ZnO.[47] Each measurement was done by applying an AC sinusoidal signal with peak to peak amplitude of 40mV over the constant applied bias with frequency varied between 0.1Hz and 10 kHz and the potential ranging from  $-0.8$  V to  $+0.8$  V.

### **3.5 X-ray diffraction**

The phase and the preferential orientation of the ZnO and the  $\text{Cu}_2\text{O}$  films were

determined by a Philips Xpert X-ray diffraction system using Cu  $K_{\alpha}$  radiation ( $\lambda=1.5418 \text{ \AA}$ ) operated at an acceleration voltage of 40kV.

### **3.6 Scanning Electron Microscopy**

Surface morphology and grain size of the ZnO and the Cu<sub>2</sub>O films were characterized by a field emission scanning electron microscope (FESEM EOL JSM-6335F) operated at 5kV.

### **3.7 UV-VIS spectroscopy**

The reflectance properties of the ZnO films were measured by a diffuse UV-VIS reflectance spectrophotometer (Cary 4000 UV-Vis spectrophotometer), whereas the IR spectra of the Cu<sub>2</sub>O films were measured by Perkin-Elmer Lambda 18.

### **3.8 Photoluminescence spectroscopy**

Room-temperature photoluminescence spectroscopy was obtained by using a 325nm laser as the excitation source. The spectra were recorded by a spectrometer (Edinburgh Instruments) equipped with a photomultiplier tube detector.

### 3.9 Electrical Characterization



Figure 18 Schematic diagram illustrates the contact points for the ZnO/Cu<sub>2</sub>O heterojunction.

The current-voltage characteristic was measured using a Keithley 2400 source meter via connecting point 1 to point 2 or point 3 shown in Figure 18. For ZnO film, silver top electrode was deposited, whereas for Cu<sub>2</sub>O film platinum top electrode was used. The deposition of the top electrodes was achieved by pulse laser deposition technique. The metal substrate and electrode form a low-resistance ohmic junction with the semiconductor electrode deposit. In such a case, a two-electrode sandwich arrangement with metal/semiconductor/metal symmetric geometry gives reasonable results. The resistivity can be calculated from the slope of the symmetric current-voltage plot in both forward and reverse bias.

### **3.10 Atomic force microscopy**

The root-mean-square surface roughnesses ( $R_q$ ) and actual film surface topologies were obtained by using an atomic force microscope (AFM, NanoScope IV, Digital Instruments). A tapping-mode was used to investigate the sample surface. The tapping mode has an advantage that the images grasped have a high correspondence.

## Chapter 4 Results and Discussions

### 4.1 Zinc Oxide

#### 4.1.1 Electrodeposition

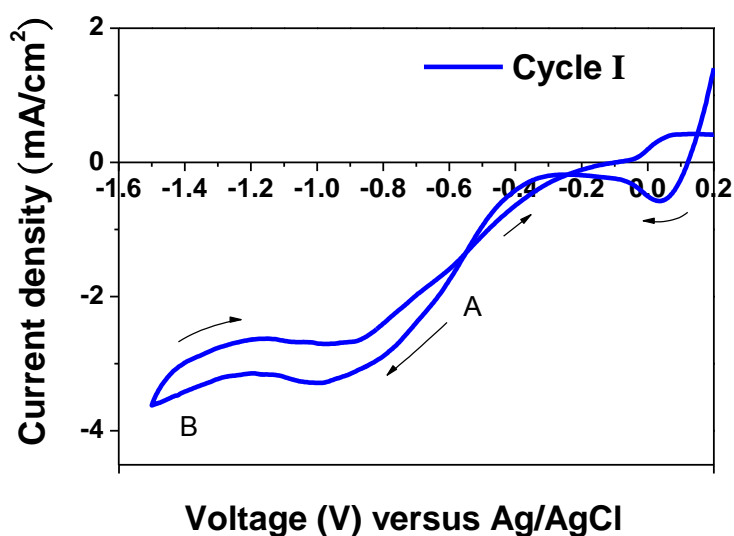


Figure 19 Cyclic voltammogram of a Cu coated PET electrode in 0.01M zinc nitrate solution with bath temperature: 80°C and pH: 3.6 .

The voltammogram in Figure 19 shows the reactions occurred on the Cu/PET substrate when it is being scanned from 0.2V to -1.5V in the zinc nitrate solution. A steep increase of cathodic current occurs at -0.4V and reaches 3.5mA at -1.0V (curve A). In this region, the reduction of nitrate ions as well as hydrogen ions contributes to the large increase of cathodic current as their reducing potentials are similar to each other. The reduction of nitrate ions generates a lot of OH<sup>-</sup> ions which help the formation of ZnO. Indeed, the reduction of nitrate ion is accompanied by the following equations:



When the potential is further decreased beyond -1.0V, a slightly increase of the cathodic current is resulted. This further increase in the cathodic current is due to a more negative potential favors the reduction of the zinc ions to zinc metal on the surface of substrate. This results in a large current flow. Therefore, the voltage range(vs Ag/AgCl) for electrodeposition of ZnO is between -0.4V and -1.0V. However, for high cathodic voltage, multi-reactions such as deposition of zinc metal might occur. Thus in our experiments, the voltage range was set between -0.4V and -0.7V.

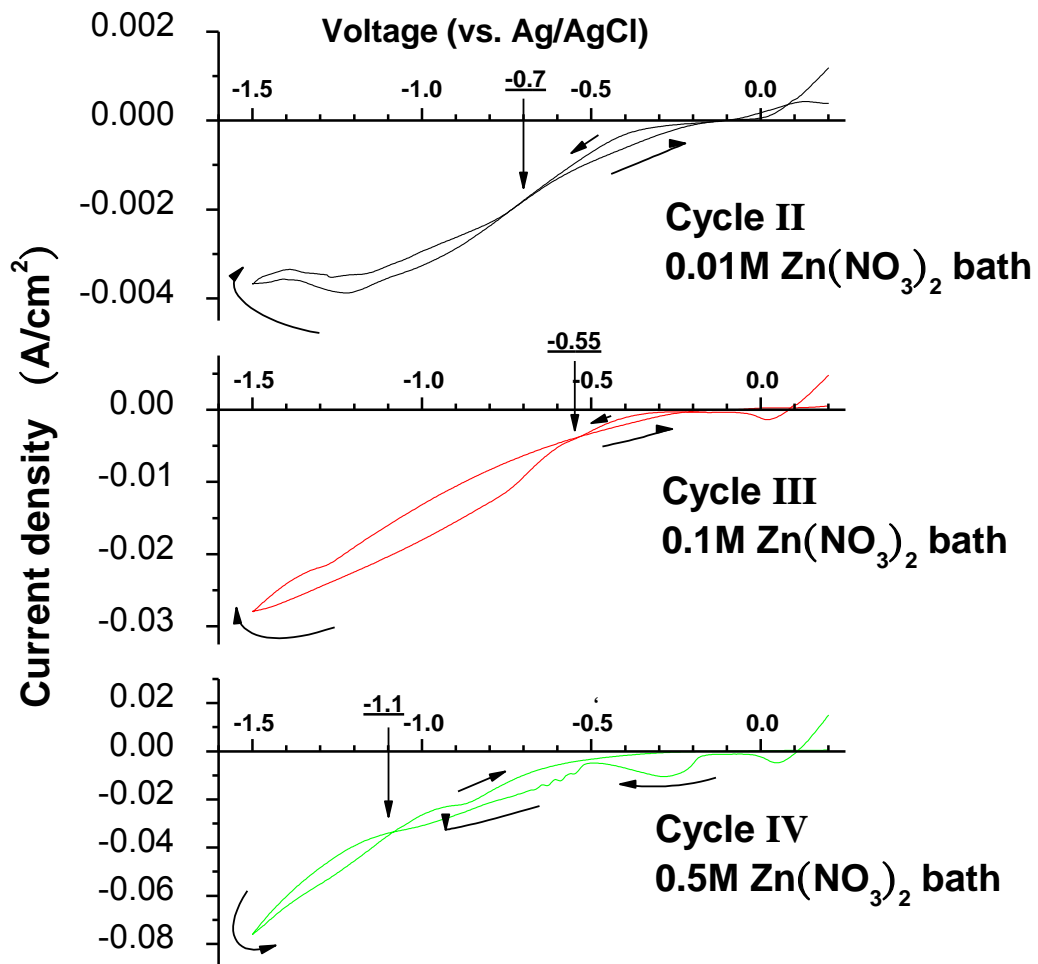


Figure 20 Effect of concentration on the cyclic voltammogram

Figure 20 shows the effects of the  $\text{Zn}(\text{NO}_3)_2$  bath concentration on the cyclic voltammograms. The crossover points (marked with arrow in the figure) of the cyclic loop shift to a more positive potential from -0.7V to -0.55V as a higher  $\text{Zn}(\text{NO}_3)_2$  concentration of 0.1M is used. Further increase the concentration to 0.5M, however, the crossover point moves back to a more negative potential side with a value of -1.1V. Since the position of the crossover point related to the potential of the nucleation[48], it implies that the nucleation of the zinc oxide begins at that particular potential. Such crossover phenomenon was also observed when a fluorine-doped tin oxide (FTO) coated glass substrate was used [48].

For concentration between 0.01M and 0.1M, nucleation potential decreases with increasing concentration. This is explained by the Nernst equation (equation 2.4) where  $E_e \propto \ln \frac{a_{\text{M}^{Z+}}}{a_{\text{M}}}$ . The increased concentration of the nitrate ions results in a more positive reducing potential. However, as the concentration increases above 0.1M, say 0.5M for sample in cycle IV, the current density does not ramp similarly with others. The current density of the backward ramping potential at -1.5V is more negative than the forward one. The origin of this crossover is likely due to the deposition of zinc metal on the working electrode when the concentration of zinc ion is too high, as indicated in Figure 19 where a high potential resulted in the deposition of Zn metal. As

a result, the crossover appear in the cycle IV voltammogram might be related to deposition of Zn metal and no crossover of zinc oxide nucleation is observed because the copper substrate is covered with a layer of zinc after the forward potential ramping. Moreover, the magnitude of the current density increases with the concentration. This logical relation can be explained by the Butler—Volmer Equation (Eq. 2.4).

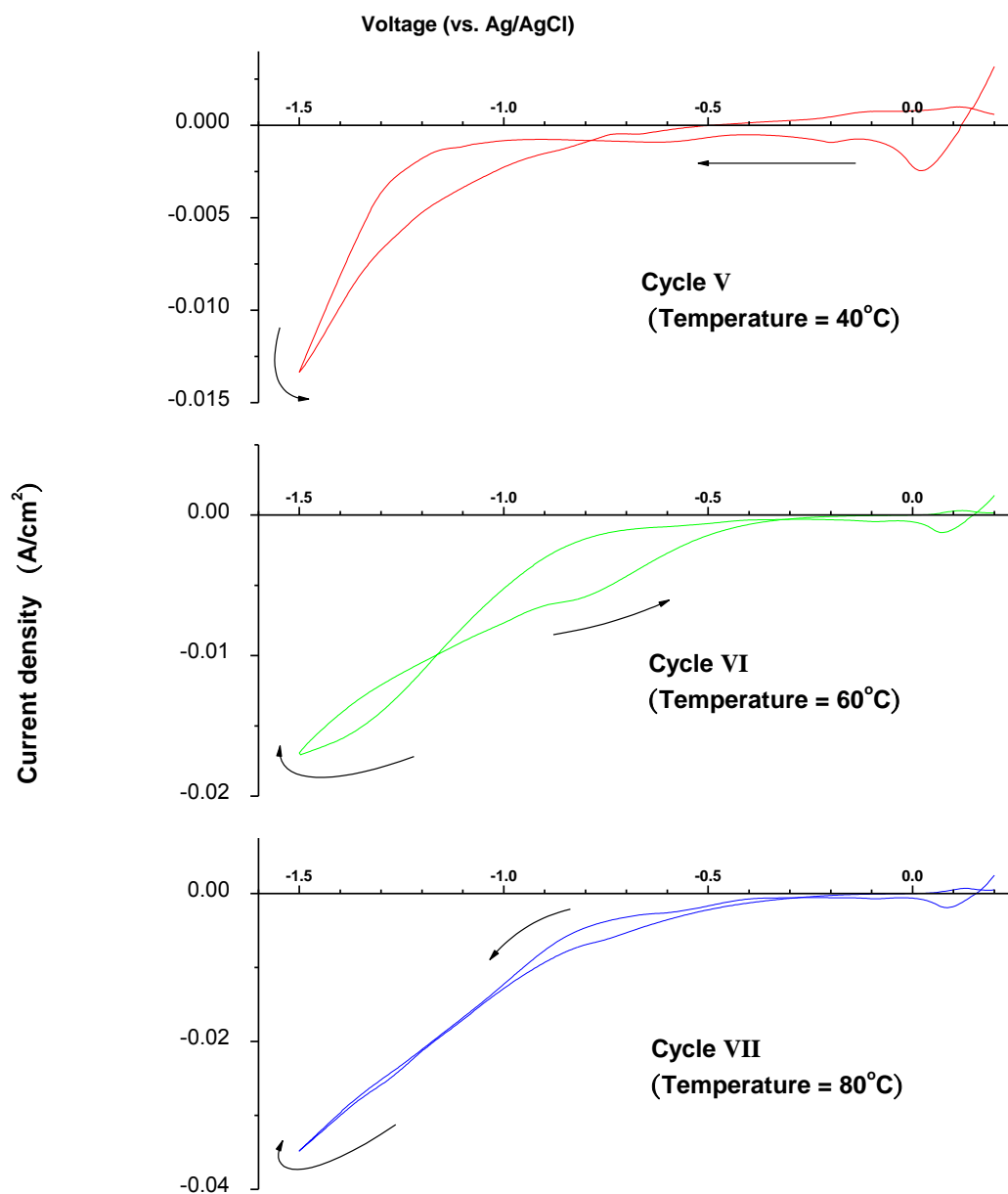


Figure 21 Effect of temperature on the cyclic voltammogram

Effects of temperature on the cyclic voltammogram of 0.1M  $Zn(NO_3)_2$  are displayed in figure 21. Firstly, decrease of deposition temperature gives a lower current density for a fixed voltage. In addition, the prolonged linear region of the forward sweeping in sample V indicates that a higher potential is needed for the reduction reaction to be occurred. Similar to sample of cycle IV, the current density of the backward ramping potential at -1.5V is more negative than the forward one. The behavior of the voltammograms of samples of cycle VI and cycle VII are very similar. The reduction reaction starts at a potential below -0.5V. Thus, for the studies of effects of temperature, samples at different bath concentration and temperature using a fixed voltage of -0.55V were employed.

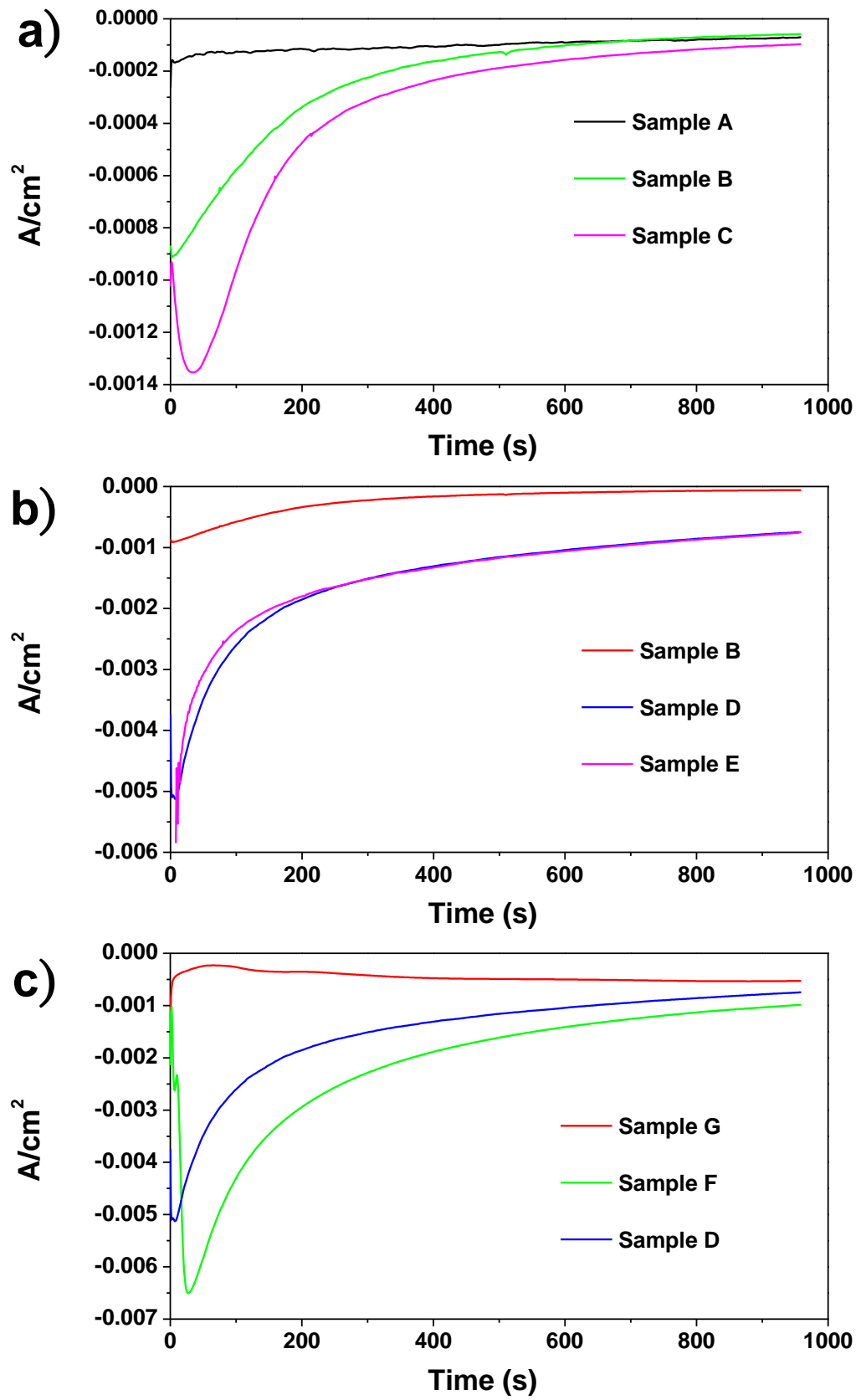


Figure 22 Chronoamperometric transient curves of the effect of a) applied voltage, b) concentrations and c) temperature.

Sample A	Sample B	Sample C	Sample D	Sample E	Sample F	Sample G
0.09719	0.21918	0.33575	1.43964	1.43895	2.05816	0.4335

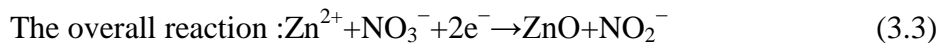
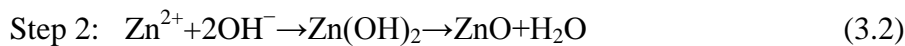
Table 4. Integration of the area under the curves with t=0s to t=960s as shown in Figure 22 ( $j \times t$ , unit:  $C\ cm^{-2}$ )

By using equation 2.3 in chapter 2,

$$\Delta m = \frac{M}{zF} j \times t$$

Here, M is the **molecular mass of ZnO** and equals to 81.408 g/mol

The chemical reactions involved in the electrodeposition of ZnO :[49]



From Equation (3.3) and assuming that all the electrons are used to produce zinc oxide, we notice that 2 mole of electrons will be consumed to produce one mole of ZnO. Thus, the mass of ZnO were calculated based on values from table 4.

Sample A	Sample B	Sample C	Sample D	Sample E	Sample F	Sample G
41	92	142	607	607	868	183

Table 5. Deposited mass per unit area of ZnO ( $\mu\text{g}\ cm^{-2}$ ) after 960s.

The negative currents recorded in Figure 22 represent the cathodic currents due to the reduction reactions occurs on the working electrode. For sample C, a dip is found at the beginning of the electrodeposition process. The shape of this peak is typical of a three dimensional electrocrystallisation growth process[50], [51]. At deposition potential of -0.7V (Sample C), the cathodic current increases to a maximum magnitude and then decreases again before reaching a constant value of ~0.2mA. This is because immediately after applying a potential, the cathodic current rapidly increases because the nucleation is instantaneous and the three-dimensional growth of each crystal rapidly increases the active surface area. The current reaches a maximum during the coalescence process. After the coalescence process, the current decreases again. Similar results were also observed in sample D and sample F. However, for other samples, the lower density of nucleation results low coalescence process. As a consequence, disappearance of the peak when nitration ion concentration decreases might be attributed to a lower density of nucleation sites as confirmed by SEM micrographs shown in Figure 24a and b.

Sample D and sample E show almost identical time profiles of the current density. This indicates that as we further increased the concentration from 0.1M to 0.5M, the deposited mass per unit area remained the same. Thus, nitrate concentration in the

electrodeposition of ZnO seems to be saturated at about 0.1M. Indeed, the formation of ZnO layer by electrodeposition relies on two successive reactions (Equations 3.1 and 3.2). The first reaction involves electron transfer. The hydroxide ions produced from the first reaction react with the Zn ions as shown in the second reaction. When a high nitrate concentration of deposition bath is employed, the hydroxide ions are more readily produced and further accumulated around the working electrode ready for the second reaction. Here, the nitrate ion possesses negative charge which has the same charge as the working electrode (cathode). Thus, the area of the electrode limits the number of nitrate ions accumulated around the electrode. Therefore, this explains why a saturated current density was observed in samples D and E.

Low temperature deposition such as sample G shows a comparatively low deposition current. It is because low temperature not only affects the experimental reducing potential ( $E_e$  in Equation 2.4) of nitrate ion but also decreases the amount of ion diffusion toward the working electrode. The current density of ZnO deposited at 60°C (sample F) is a little bit higher than that of ZnO deposited at 80°C (sample D). The current peak of sample F is higher and occurs later than sample D, implying that the number of nucleation site of ZnO in sample F is more than that in sample D. Based on our studies, the optimal temperature for the growth of ZnO using electrodeposition

technique is 80°C

#### 4.1.2 Structural Properties

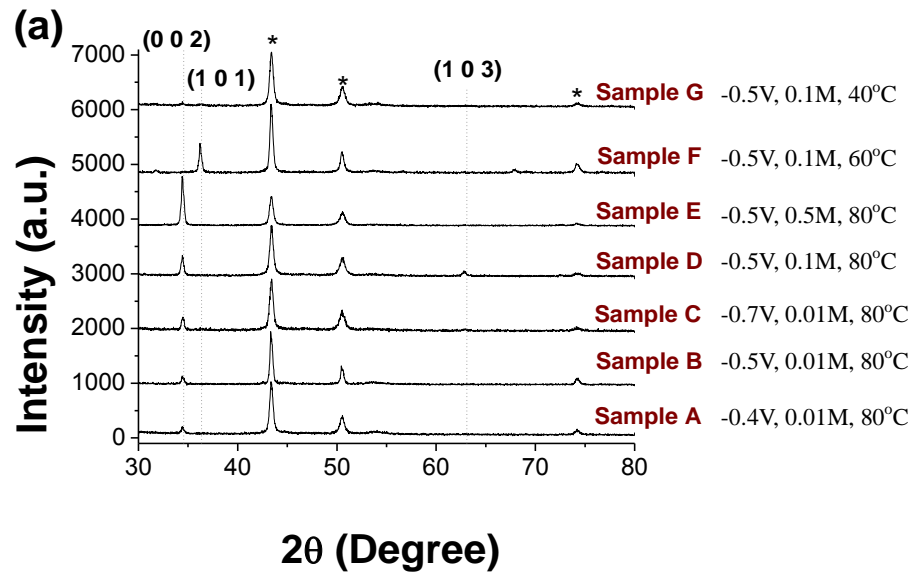


Figure 23 X-ray theta-2 theta scans of the prepared ZnO films. (\* represents the diffraction peaks from Cu-coating.)

The X-ray diffraction patterns of samples A, B and C obtained at cathodic potentials of -0.4V, -0.5V and -0.7V respectively are shown in Figure 23. The depositions temperature and zinc nitrate concentration were maintained at 80°C and 0.01M, respectively. As shown in Figure 23, only (0 0 2) peak is observed, indicating that these sample possess good crystalline with highly oriented ZnO crystal. The strong preferential growth habit is explained by the fast growth kinetics of  $\langle 0001 \rangle$  among all directions [52]. Comparing these 3 samples, increasing the cathodic potential of the

working electrode results in a stronger (0 0 2) peak intensity of ZnO in XRD. It implies that more ZnO crystals are synthesized when a higher potential is applied. Hence, one of the major rate-determining factors of the electrodeposition was applied cathodic voltage.

On the other hand, the effect of increasing the concentrations of zinc nitrate solution on the structural properties is revealed by comparing samples B, D and E. Generally speaking, as the bath concentration increases, the relative intensity of the (002) peak (as compared to the Cu peaks) is increased. Furthermore, the full width at half maximum (FWHM) of the (002) peak remains the same. This indicates that higher concentration results in faster growth of ZnO while the preferential orientation remains the same. Similar, nitrate concentration is also another rate-determining factor of the electrodeposition.

Finally, when the bath temperature is decreased to 60°C, the dominant peak changes from (002) to (101) as shown in the XRD pattern of sample F in Figure 23. Further decrease the bath temperature to 40°C, no detectable crystalline ZnO is observed. Thus the threshold temperature for the electrodeposition is above 40°C.

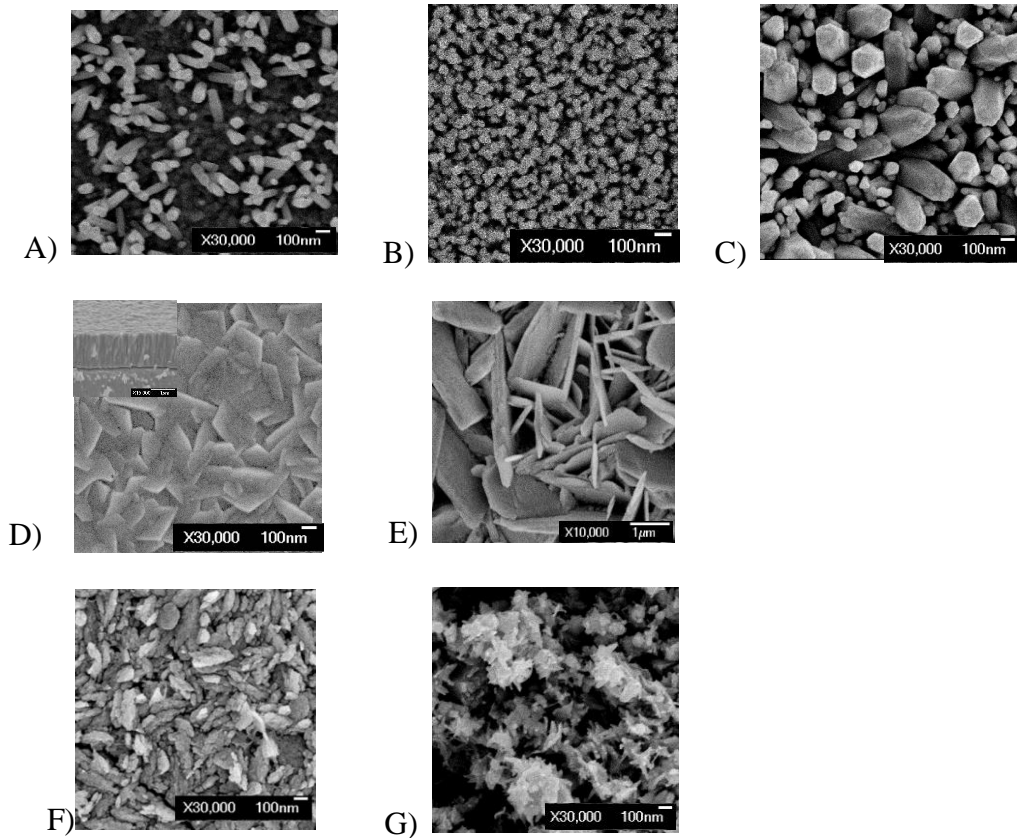


Figure 24 SEM micrographs of the ZnO films prepared by varying deposition potentials, bath concentration and bath temperature (from left to right): sample A to C (first row), sample D and sample E (second row), sample F and sample G (third row).

Figures 24 (A) to (G) summarize the effects of applied voltage, bath concentration and deposition temperature on the surface morphology of the fabricated ZnO films. Generally speaking, ZnO nano-rods or crystals of various sizes are deposited on the substrates with different applied potentials, concentration and temperature as shown in Figure 24. The diameter of the rods is increased from  $\sim 50\text{nm}$  to  $\sim 200\text{nm}$  as the deposition potential changing from  $-0.4\text{V}$  to  $-0.7\text{V}$ , respectively. Furthermore, a more negative deposition potential results in an increase of rod density as shown in the

figures. This also explains why a stronger XRD peak was obtained in the XRD patterns. On the other hand, higher concentration of zinc nitrate electrolyte produces a denser ZnO films (Figures 24 (B), (D), (E)). Besides a denser film, hexagonal grains with size of 300nm instead of nanorods are obtained at high concentration. Further increasing the concentration to 0.5M, nodular ZnO grains appear as observed in Fig. 24 (E). The plate-like crystals,  $\sim 3\mu\text{m}$  in size, are randomly aligned and their c-axis orient perpendicular to the substrate surface (as demonstrated in the XRD results). Finally, surface morphologies of the deposited ZnO at 40°C and 60°C are shown in Figures 24 (G) and 24 (F). Deposition of ZnO at 60°C (sample F) favors the growth of nano platelet-like crystals which are approximately 100nm in size. Further decrease the growth temperature to 40°C, aggregation of ZnO hexagonal slices forms irregular columns and some pores are located between columns. As suggested by XRD, these nano ZnO hexagonal slices are probably amorphous in nature. Based on the SEM micrographs, the ZnO film electrodeposited from 0.1M zinc nitrate bath was dense enough so that the studies of effects on samples deposited at different temperature using a fixed bath concentration of 0.1M were employed.

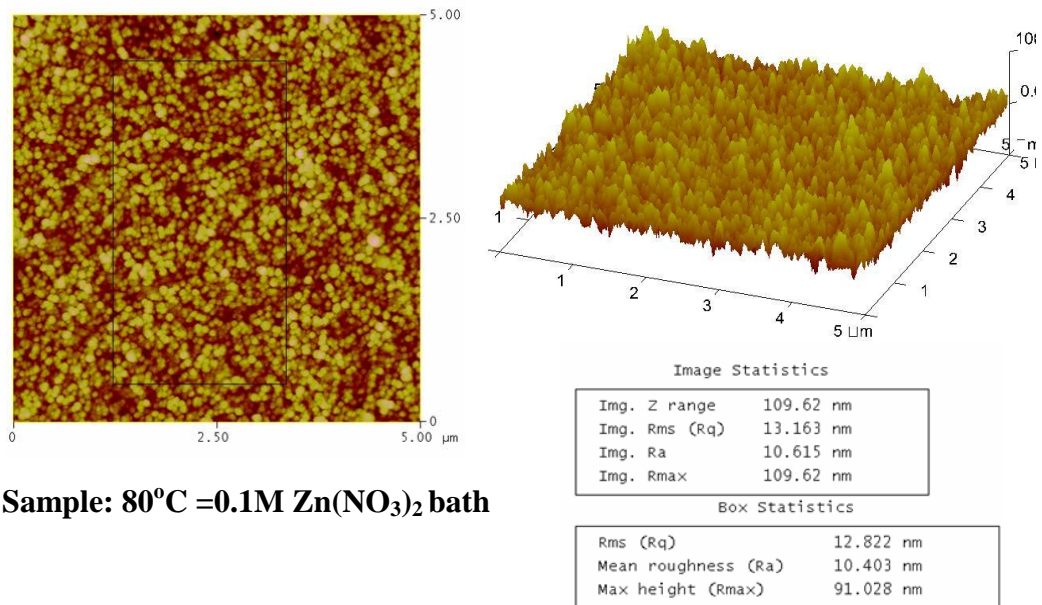


Figure 25 AFM micrographs of ZnO thin films deposited on Cu-coated PET (sample D)

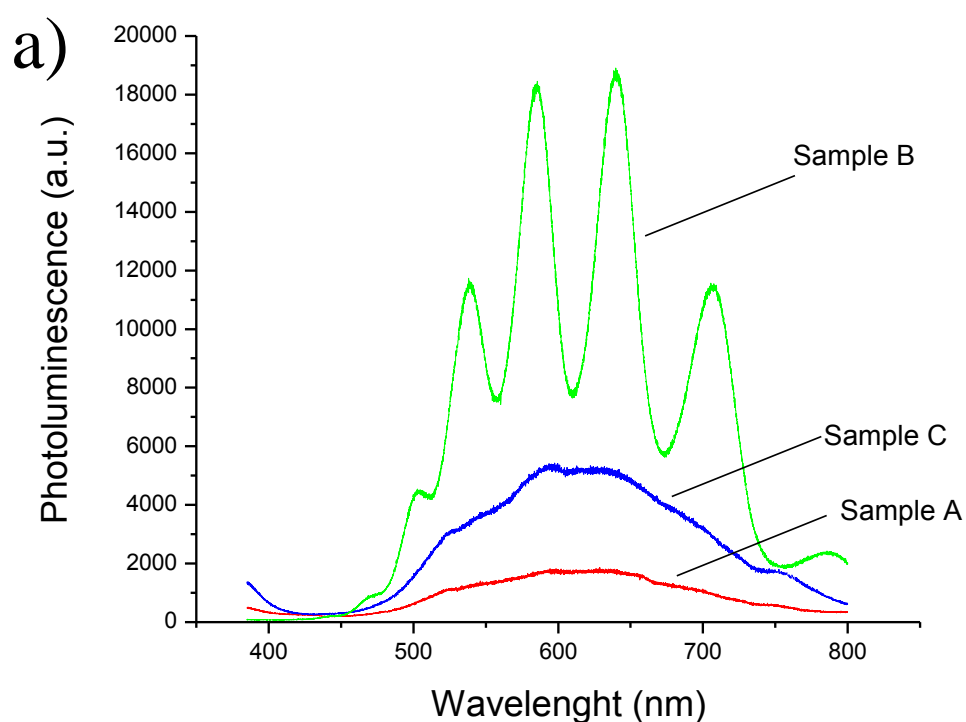
A typical AFM images obtained from sample D is shown in Figure 25. It is noticed that the root mean square surface roughness ( $R_q$ ) of this ZnO thin film is  $\sim 13$  nm which is relatively low as compared to other electrodeposited samples with roughness around 22~28nm [24]. Table 6 shows the root-mean-square roughness ( $R_q$ ) and mean roughness ( $R_a$ ) of all the samples. The roughness of samples A, C and E are too large as observed in SEM micrographs. Indeed, we have measured the surface roughness of these samples using AFM, the roughnesses obtained were over the maximum range of our AFM. For samples B and D, it seems that the processing parameters for these two films result in flat thin films. General speaking, high temperature is favor for the formation of a smoother thin film as we compared samples D, G and F. Although sample G is suspected to be an amorphous ZnO, roughness of  $\sim 70$  is obtained. It

might be due to the inhomogeneous growth of ZnO dendrite in-between the amorphous surface.

Samples	$R_q$ (nm)	$R_a$ (nm)
A	-	-
B	15.657	12.299
C	-	-
D	13.163	10.615
E	-	-
F	39.483	29.617
G	86.829	67.752

Table 6. Root-mean-square ( $R_q$ ) and mean ( $R_a$ ) roughness of all the samples.

### 4.1.3 Optical Properties



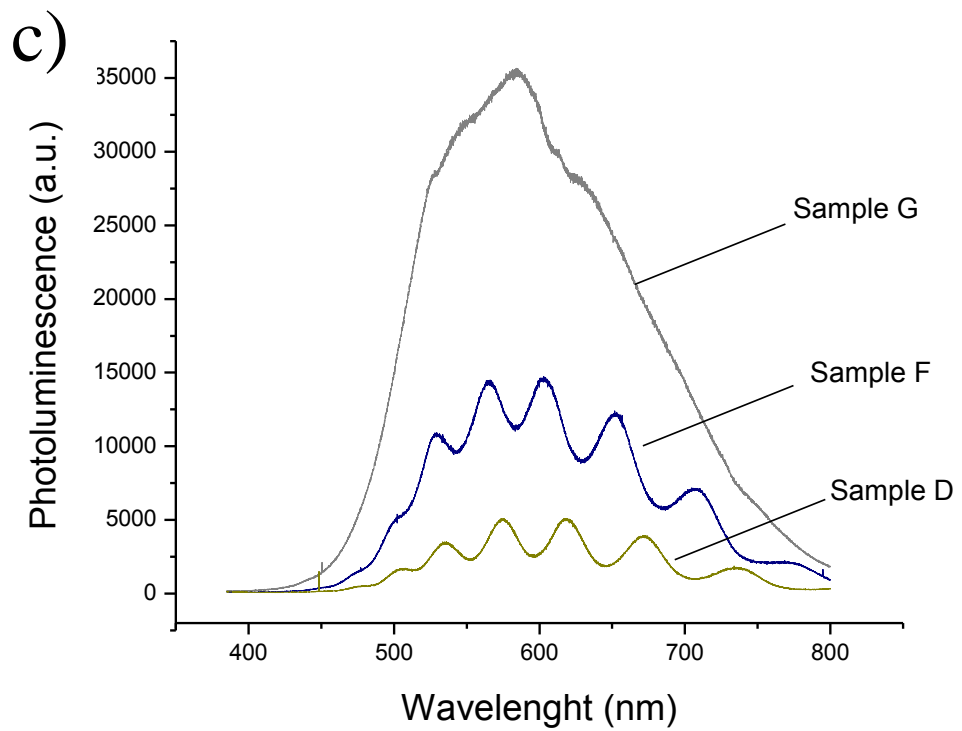
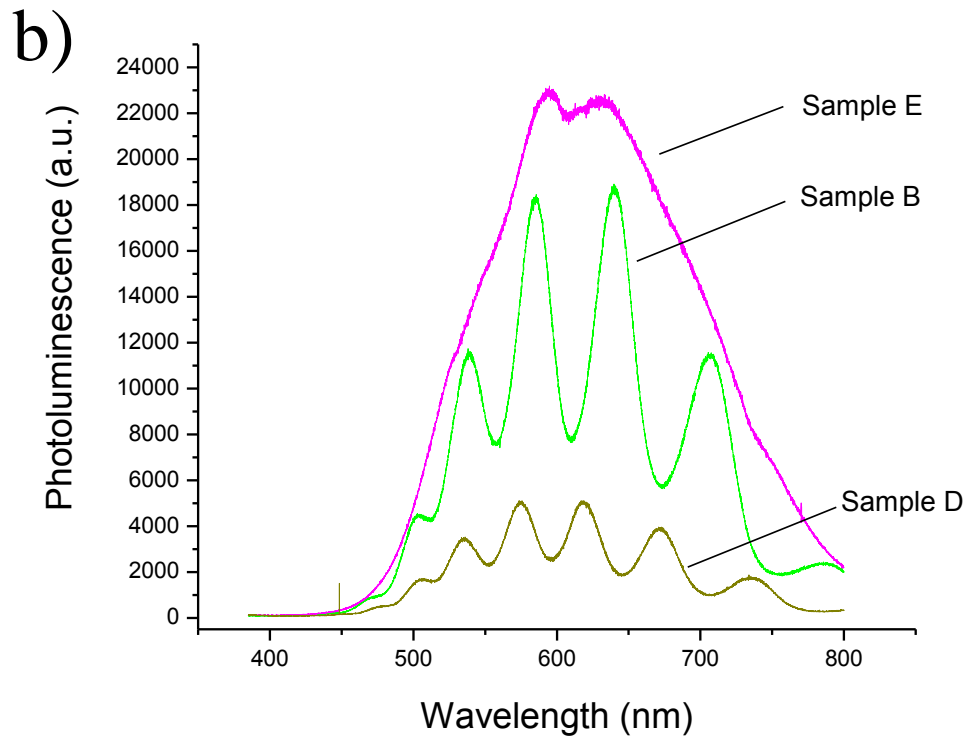


Figure 26 Photoluminescence spectra of (a) samples A, B and C (varying cathodic deposition voltage) (b) samples B, D and E (varying deposition bath concentration) and (c) samples D, F and G (varying deposition temperature).

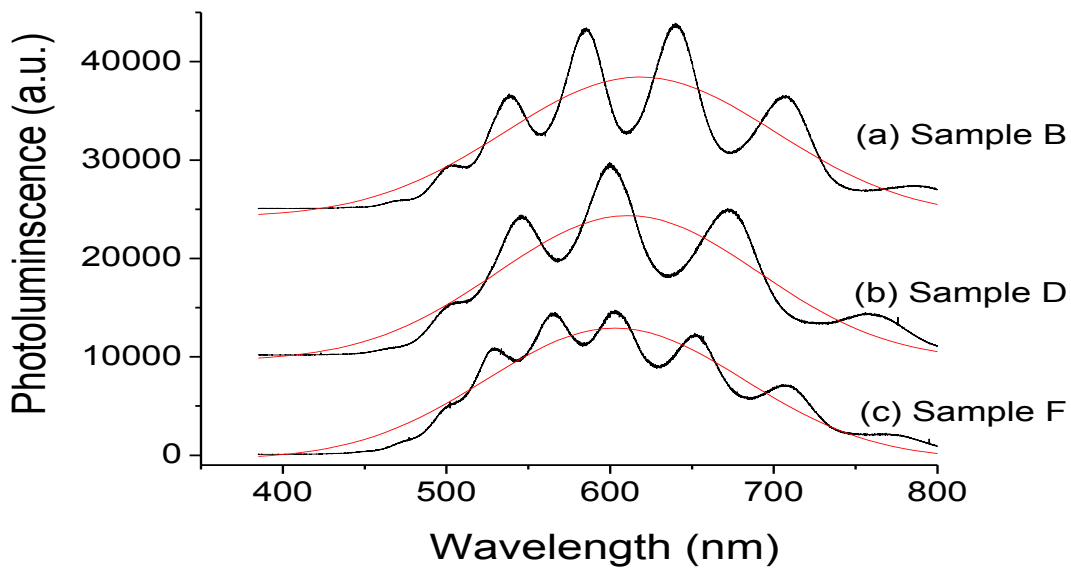


Figure 27 Photoluminescence spectra of (a) sample B, (b) sample D and (c) sample F. Red lines: Gaussian fitting for each curve.

Figure 27 shows the PL spectra of our samples. For samples B, D and F, they consist of two main features. One broad Gaussian profile with a well-structured and smooth oscillation on top of this broad Gaussian profile. Their broad emissions are fitted as shown by the red lines (Figure 27). On top of this broad profile, the well structured and smooth oscillations of the photoluminescence profiles indicated that the films have flat surfaces and uniform thicknesses. This well oscillated pattern is likely arisen from the interference between the reflected light from the top layer as well as the bottom layer of the ZnO films.

Table 7 shows the peak values of the broad emission profiles for different samples. From the experimental data, it seems that we cannot make a direct correlation between applied voltage and bath concentration with the peak value of the broad band. More experimental results will be needed before we can reveal the correlation. For the samples A to E (Figures 26a and 26b), they show a broad yellow emission feature with a peak at ~615nm in Figure 26a. It is previously assigned as the emission induced by oxygen interstitials [11]. Deposition of ZnO film at 60°C (sample F) causes the defect emission shift from yellow to green peaking at 602nm. This 602nm peak was previously assigned to be arisen from oxygen deficiency [11]. However, decreasing the deposition temperature induce the blue shift of the broad band from ~615nm to 584nm. It implies the defects of the ZnO films are changing from oxygen interstitials to oxygen vacancy.

Table 7. The broad band peak value of different samples obtained from their PL spectra.

<b>Sample</b>	<b>Peak (nm)</b>
A	615
B	618
C	613
D	613
E	615
F	602
G	584

Obvious oscillations were observed in the PL spectra of the smooth sample B, D and F in Fig. 26. Its origin is ascribed to the interference between the reflection from the top and bottom layers of the ZnO film. Similar interferences have been observed in other zinc oxide films [53]. The observed oscillations in PL spectra carry very rich information, for example, the thickness of the film, the refractive index or porosity of the deposit[54].

The general equation to determine the separation between two longitudinal modes within a Fabry–Pérot cavity is expressed as follows:

$$\Delta\lambda = \frac{\lambda^2}{2L[n - \lambda \frac{dn}{d\lambda}]} \quad (3.1)$$

where  $\lambda$  is the wavelength,  $L$  is the thickness of the film observed by SEM,  $n$  is the refractive index of the film, and  $dn/d\lambda$  is the materials dispersion.

Here, we assumed that the dispersion ( $dn/d\lambda$ ) is zero in the spectral range studied (between 1.9–2.9 eV) because for ZnO  $\Delta n$  is small within the spectral range. In addition, the  $\lambda$  we are interested is around the band-gap of ZnO. Thus Eq. 3.1 can be simplified to:

$$\Delta E = \frac{hc}{2nL} \quad (3.2)$$

The data obtained in the observed oscillations are listed as below:

<b>Sample B</b>			
Peak (nm)	Peak (eV)	Difference between two peaks (eV)	Reflective index
538	2.304833	0.185175	1.85776
585	2.119658	0.179126	1.920491
639	1.940532	0.184158	1.868014
706	1.756374		AVG= 1.882088

Film thickness = 1.803 $\mu$ m

<b>Sample D</b>			
Peak (nm)	Peak (eV)	Difference between two peaks (eV)	Reflective index
535	2.317757	0.157478	2.108479
574	2.160279	0.150554	2.205448
617	2.009724	0.161736	2.052968
671	1.847988	0.160913	2.06347
735	1.687075		AVG = 2.107591

Film thickness = 1.868 $\mu$ m

Sample F			
Peak (nm)	Peak (eV)	Difference between two peaks (eV)	Reflective index
528	2.348485	0.149903	2.433922
564	2.198582	0.135354	2.695554
601	2.063228	0.161387	2.260727
652	1.90184	0.147951	2.466042
707	1.75389		AVG= 2.4641

Film thickness = 1.697 $\mu$ m

The periodicity of each sample varies from  $\Delta E \sim 150$  meV to 185 meV. The refractive index of sample B, sample D and sample F are deduced to be 1.88, 2.10 and 2.46 respectively. Only the value from sample B agrees quite well with the literature (about 1.80–1.98), while values from sample D shows a little deviation. The serious deviation of sample F may due to the faulted assumption of equation 3.2.

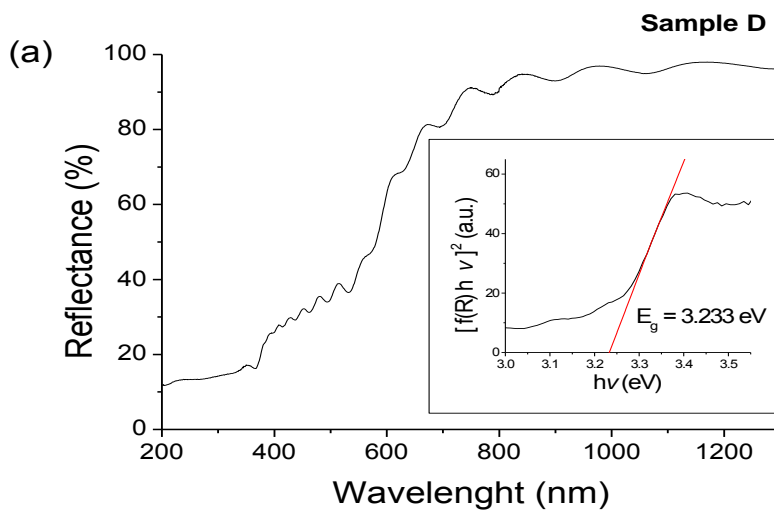


Figure 28 Diffuse UV-Vis reflectance spectrum and Kubelka-Munk transformed reflectance spectrum (inset) of deposited ZnO film on Cu-coated PET (sample D).

<b>Samples</b>	<b>Bandgap of ZnO (eV)</b>
A	3.17
B	3.24
C	3.19
D	3.23
E	3.18
F	3.25
G	3.36

Table 8. The bandgap of different samples calculated from diffuse UV-Vis reflectance spectrum via Kubelka-Munk transformation.

Diffuse reflectance measurements in the wavelength range of UV-visible–near-infrared have been carried out in order to determine the band gap energies of ZnO films. The diffuse reflectance spectra of the samples are shown in Figure 28. General speaking, all the ZnO films show similar profiles. They exhibit about 90% reflectance from 600nm to 1200nm. Similar to the PL spectra, the well structured and smooth oscillations of the profiles indicate that the films have flat surfaces and uniform thicknesses. A considerable reduction in reflectance starts at about 600 nm. This steep drop is relative to the band gap absorption of the ZnO. The diffuse reflectance spectrum of sample D after Kubelka-Munk treatment is shown in the inset of Figure 28. The bandgap of this

sample can be determined from the intersection between the linear fit and the photon energy axis using equation 2.16. Bandgap values of all the samples obtained by this method are given in Table 8. Sample B, D and F possess a value of 3.24eV, 3.23eV and 3.25eV, respectively, which is close to 3.3eV obtained in literature. The bandgap of samples A, C and E are mainly lying around 3.18eV. For the sample G, which possesses the worst crystalline structure as observed in SEM micrograph, its bandgap is blue shift to 3.36eV. Such blue shift in band gap energy of ZnO was also demonstrated by Tan et al. and Khoshman et al. who fabricated amorphous ZnO by chemical vapor deposition and RF magnetron sputtering, respectively.

#### 4.1.4 Electrical Properties

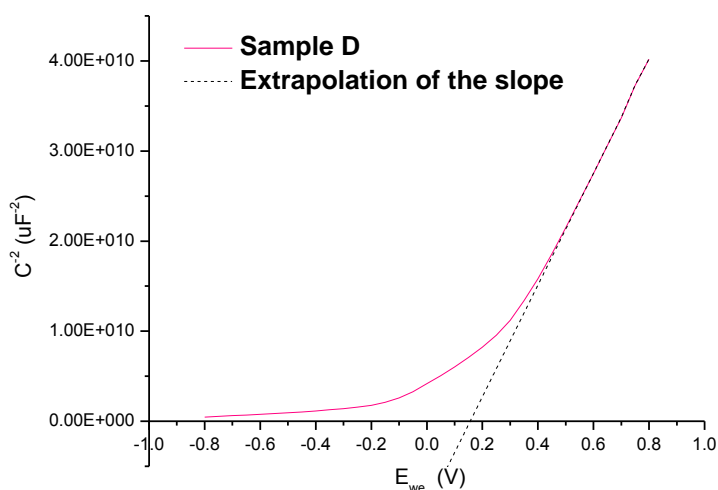


Figure 29 Mott-Schottky plots of ZnO in sample D. Solid lines represent the fits of the experimental data employing Eq.2.6, and the dashed line represents the fitting curve.  $E_{we}$  is the voltage between the reference electrode (Ag/AgCl in sat' KCl) and the voltage of working electrode.

Figure 29 shows the experimental Mott-Schottky plot for sample D. The data presents a linear-like behavior indicating a high donor density. Based on the graph, the slope of the extrapolation is 0.157V, thus the obtained  $N_D = 4.9 \times 10^{18} \text{ cm}^{-3}$ . The method shown here allows us to determine the donor density of our samples with high accuracy. The observed donor density in our experiments is similar to the values reported from ZnO films fabricated by vapor phase techniques ( $10^{17} - 10^{18} \text{ cm}^{-3}$ ). [55], [56] For sample C, a very high electron donor concentration of order of  $10^{21} \text{ cm}^{-3}$  is recorded. Such high electron concentration can be accounted by zinc incorporation due to a high deposition voltage. It results the non-ideality of semiconductor/electrolyte interface by the presence of energy states associated with the surface that are different from those in the interior of the semiconductor. These surface states act as channels for electron transfer, if they lie at the appropriate energy. Another postulation is that the large defects states in ZnO film contribute to the high donor concentration, which can be seen in the broadband emission of the PL spectrum (in Figure 26).

Samples	Electron donor concentration of ZnO ( $\times 10^{18}\text{cm}^{-3}$ )	
A		33
B		140
C		1300
D		4.9
E		0.049
F		16
G		6.3

Table 9. The carrier concentration (electron donor) of different samples calculated from their respective Mott-Schottky plot.

## 4.2 Cuprous Oxide

### 4.2.1 Electrodeposition

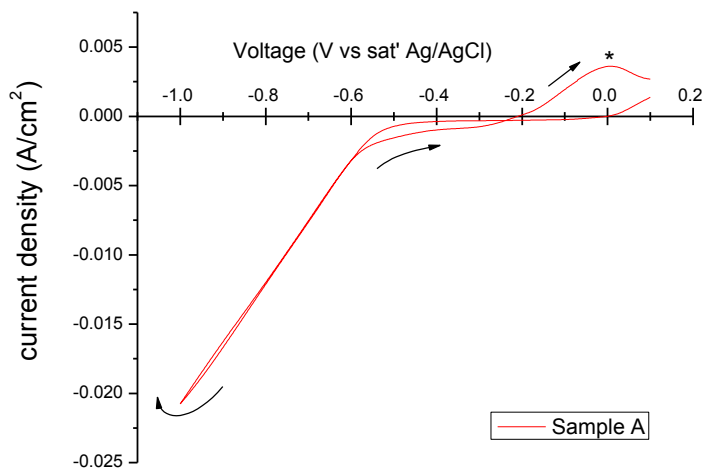
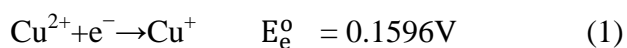


Figure 30 Voltammogram on copper-coated PET in 0.45 M  $\text{CuSO}_4$ , 3.25M lactic acid and NaOH.

Scanned rate is  $20 \text{ mV s}^{-1}$ , pH is 10.0 and temperature is  $40^\circ\text{C}$ .

The electrolyte used in the cyclic voltammetric studies of the growth of cuprous oxide on Cu-PET substrates contained copper sulfate (0.45 M), lactic acid(3.25 M) and NaOH pellets. Figure 30 shows the typical scanning curve between 0.1 V and -1.0 V. By sweeping towards the negative potential side, a steep increase in current is obtained at cathodic potential of -0.6V corresponding to the reduction of Cu ions into copper metal as its standard reduction potential ( $\text{Cu}^{2+} + 2\text{e}^- \rightarrow \text{Cu}$ ,  $E^\circ = 0.34\text{V}$ ) is more negative than the reduction potential of  $\text{Cu}_2\text{O}$  formation. This potential value is very similar to the equilibrium potential for  $\text{Cu}_2\text{O}/\text{Cu}(0)$  system at pH 13.2[49].The crossover occurred at -0.23V. This implies that the nucleation of  $\text{Cu}_2\text{O}$  crystal occurs around this voltage.

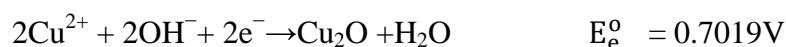
It is suggested that formation of cuprous oxide proceeds in two steps.[57] The first step involves the reduction of copper(II) ( $\text{Cu}^{2+}$ ) ions to copper(I) ( $\text{Cu}^+$ ) in the solution. This involves the breakdown of copper-lactic complex:



Then, the formed  $\text{Cu}^+$  ions undergo a hydrolysis reaction to become  $\text{Cu}_2\text{O}$ :



Combining the two equations, the overall reaction is:



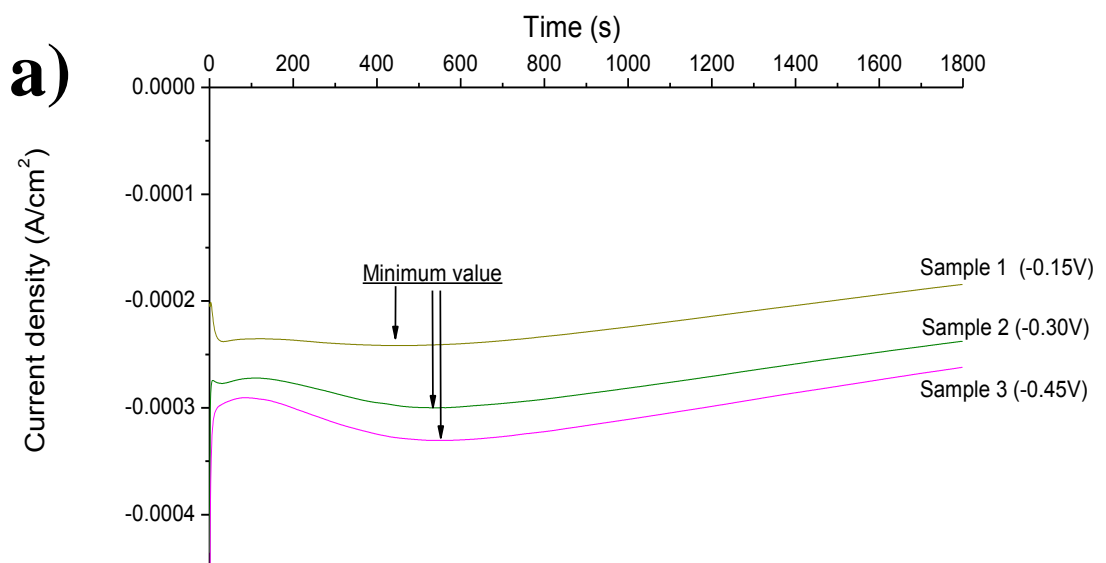
It is noticed that the deposition potential is pH sensitive (using the Nernst equation (Equation 2.4) to calculate,  $E_e = -0.2\text{ V}$  for pH of 7.0 and  $-0.45\text{ V}$  for pH of 9.0, indicating the change in pH versus change in potential =  $125\text{ mV/pH}$ ).

During the reverse potential scan, there is a crossover of the cathodic and anodic sweeping (mark with an arrow in Figure 30). This implies that formation of a solid phase involving nucleation process is happened at around  $-0.25\text{V}$ . As expected, a sharp anodic peak appears ( $E_p = -0.01\text{ V}$ ) related to the oxidation of the as-grown  $\text{Cu}_2\text{O}$  (marked with an \*). Careful analysis of the CV pattern leads us to select an optimum deposition potential in the range of  $-0.1\text{ V}$  to  $-0.7\text{ V}$  to grow  $\text{Cu}_2\text{O}$  thin films.

Cuprous oxide films deposited potentiostatically on Cu/PET are found to be thick and uniform with reddish brown in appearance. The effects of deposition potential and deposition time on the deposition process are shown in Figure 31. From Figures 31a and 31b, the reaction rate increase with the applied cathodic voltage. The same trend, which involves a minimum in its current transient curve, is noted for films prepared at

all potentials. As the deposition voltage increases, the magnitude of minimum current density value increases and appears at a longer deposition time i.e. at a later time. Since the appearance of the current density relates to the nucleation process of the solid state sample[58], our results indicate that the amount of nucleation in sample 3 is larger than those in samples 1 and 2. For sample 4, 5 and 6, the minimum current density disappears as the applied potential sufficiently high enough so that the electro-double layer charging on the sample surface distort such phenomenon.[59]

In figure 31c, the peak in the current transient curve is more negative. At the end of deposition of each sample, however, they have the same current density. Since the same deposition voltage was employed, it is normal to have the same level of current density.



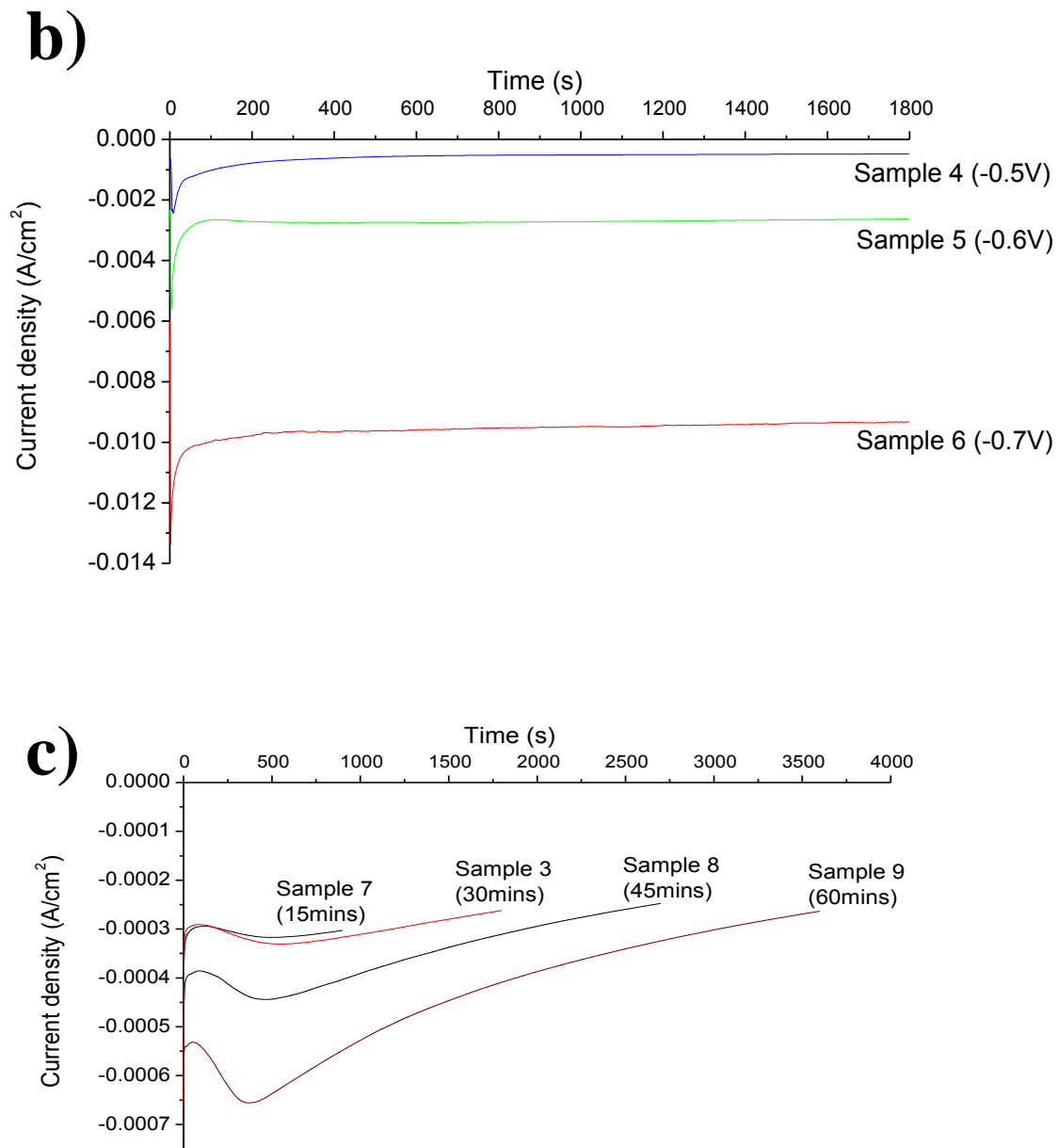


Figure 31 Chronoamperometric transient curves of the effect of a) applied voltage of sample 1 to 3, b) applied voltage of sample 4 to 6 and c) deposition time.

Sample 1	Sample 2	Sample 3	Sample 4	Sample 5	Sample 6	Sample 7	Sample 8	Sample 9
0.399	0.496	0.545	1.079	4.905	17.221	0.278	0.946	1.553

Table 10. Integration of the area under the curves shown in Figures 30 ( $j \times t$ , unit: C cm<sup>-2</sup>)

By using Equation 2.3 in Chapter 2,

$$\Delta m = \frac{M}{zF} j \times t$$

**Molecular mass of Cu<sub>2</sub>O (M) :143.09 g/mol**

**Electrons consumed to produce one mole of Cu<sub>2</sub>O (z) : 2**

Assuming all the electrons are used to produce cuprous oxide. Then the overall mass of

Cu<sub>2</sub>O deposited on Cu/PET are:

Sample 1	Sample 2	Sample 3	Sample 4	Sample 5	Sample 6	Sample 7	Sample 8	Sample 9
0.296	0.368	0.404	0.800	3.637	12.769	0.206	0.701	1.152

Table 11. Mass of Cu<sub>2</sub>O deposited (mg cm<sup>-2</sup>).

## 4.2.2 Structural Properties

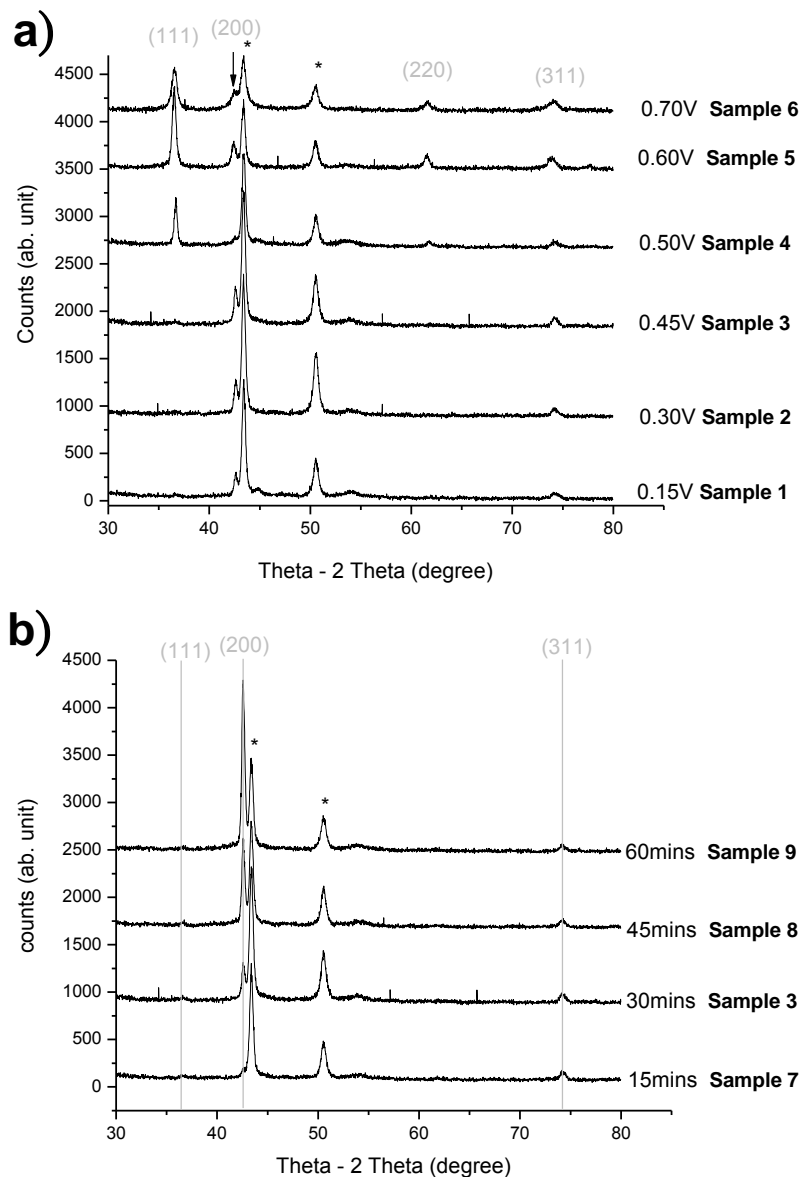


Figure 32 XRD patterns of  $\text{Cu}_2\text{O}$  films deposited at: (a) various applied cathodic potentials, sample 1 to sample 6; (b) different deposition times, sample 7 to sample 9. (\* represents the diffraction peaks from Cu-coating.)

Cuprous oxide ( $\text{Cu}_2\text{O}$ ) thin films deposited at various bath conditions are found to be polycrystalline with simple cubic structure. The effects of deposition potential on the structure of  $\text{Cu}_2\text{O}$  films were studied using X-ray diffraction analysis. Figure 31 shows

the XRD patterns of cuprous oxide thin films prepared at various deposition potentials at a solution of pH 10.0 and bath temperature 40 °C.

It is observed from the XRD patterns (Figure 32a) that the films deposited between -0.15 V and -0.45 V possess Cu<sub>2</sub>O crystal with a preferential orientation of (200). On the other hand, for films deposited at or above -0.5 V, preferential orientations of (111) are observed. Besides (111) orientation, orientations of (220) and (200) also exist in these Cu<sub>2</sub>O films, demonstrating the polycrystalline nature. The XRD results imply that for high cathodic potential, a high growth rate is resulted, as shown in Table 8. This high growth rate favours the growth of grains with multi-orientations.

Since copper substrates were used, the Cu layer that obtained during the electrodeposition process cannot be distinguished from the Cu layer already existed on the substrate. Indeed, when comparing the samples deposited at -0.6V and -0.7V, it is noticed that the ratio of orientation of (111) from Cu<sub>2</sub>O to the peaks from Cu is decreased in sample 6 as compared to sample 5. This decrease of intensity of (111) peak might be accounted by the co-deposition of Cu metal into the film. However, further experiments such as X-ray photoelectron spectroscopy should be performed in order to reveal the detail mechanism.

Figure 32b shows the correlation between the deposition time and the structure of  $\text{Cu}_2\text{O}$  when a deposition potential of  $-0.45\text{V}$  was used. The longer the deposition time, a more intense signal in the orientation of (200) is obtained. This indicates that a thicker film contains more  $\text{Cu}_2\text{O}$  crystals is obtained.

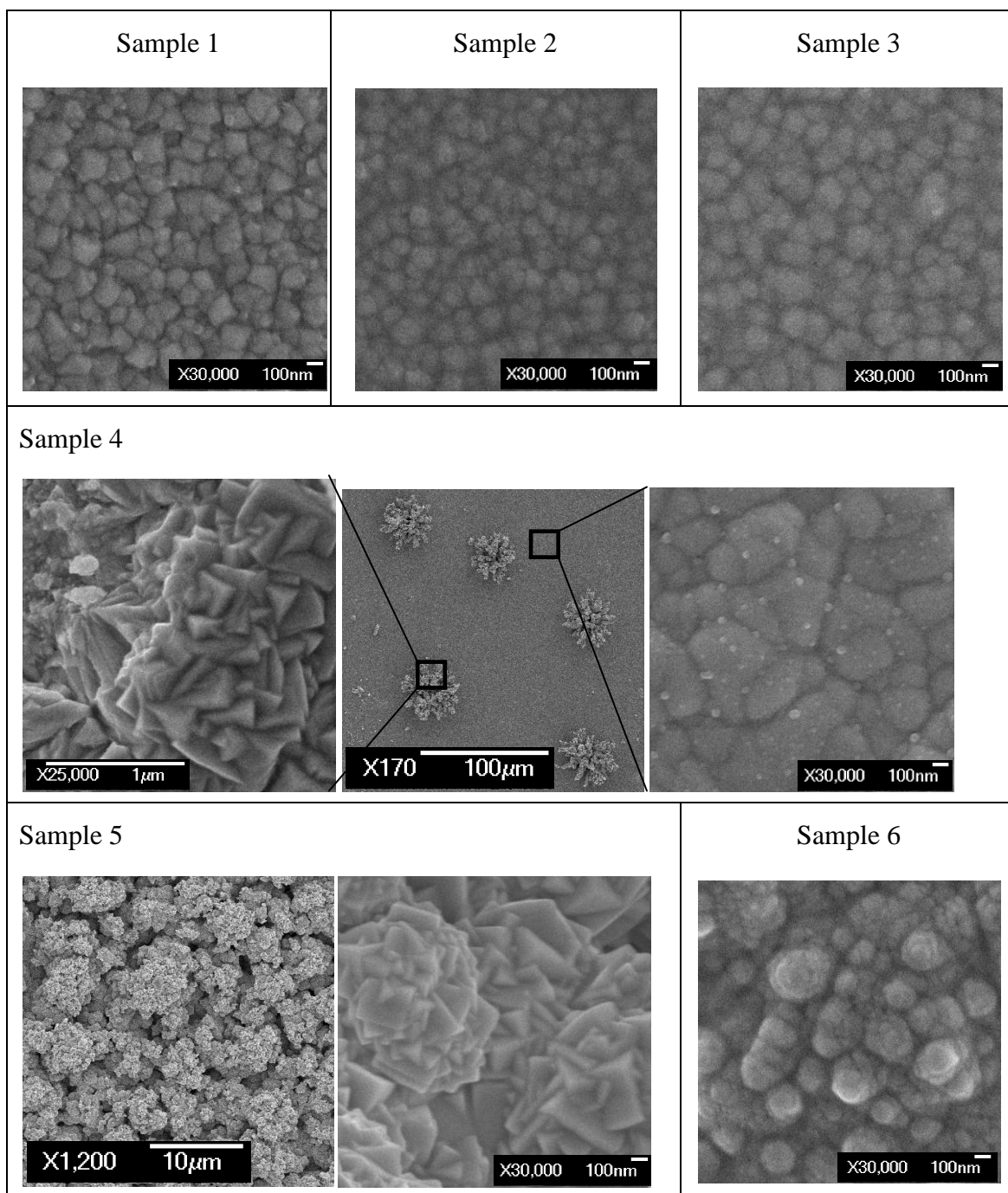


Figure 33. SEM micrographs of the  $\text{Cu}_2\text{O}$  films prepared by varying the deposition potentials.

Scanning electron micrographs obtained for  $\text{Cu}_2\text{O}$  films deposited at different potentials are shown in Figure 33. The films are polycrystalline in nature as demonstrated by XRD patterns and the surface morphology is found to be voltage

dependent. It is observed that  $\text{Cu}_2\text{O}$  films deposited at the range of  $-0.15\text{V}$  to  $-0.45\text{V}$  (first row of Figure 32) exhibit smooth and densely packed semi-spherical  $\text{Cu}_2\text{O}$  grains with size around  $100\text{nm}$ , whereas for film deposited at  $-0.5\text{V}$  (sample 4) it is noticed that some additional large dendrites with a three-sided pyramid structure are formed. These dendrites grow on the  $\text{Cu}_2\text{O}$  surface which possess clear grain boundaries similar to sample 3. Further increase the deposition voltage to  $-0.6\text{V}$  results in more dendrites growth. Finally, when the deposition voltage reaches  $-0.7\text{V}$ , the morphology changes into a rough surface with spheres embedded inside. It is suggested by XRD results that Cu metals are incorporated in sample 6 during the electrodeposition process.

The effect of deposition time on film's morphology is shown in Figure 34. When the deposition process was carried out for 15 minutes (sample 7), a dense surface is formed with a small grain size of  $\sim 100\text{nm}$ . With increasing deposition time, the grains grow in size, resulting in a more dense film. For example, the grain size becomes  $\sim 200$  to  $300\text{nm}$  in sample 9. From the SEM cross-section micrograph, the thickness of sample 9 is around  $1.4\mu\text{m}$  thick.

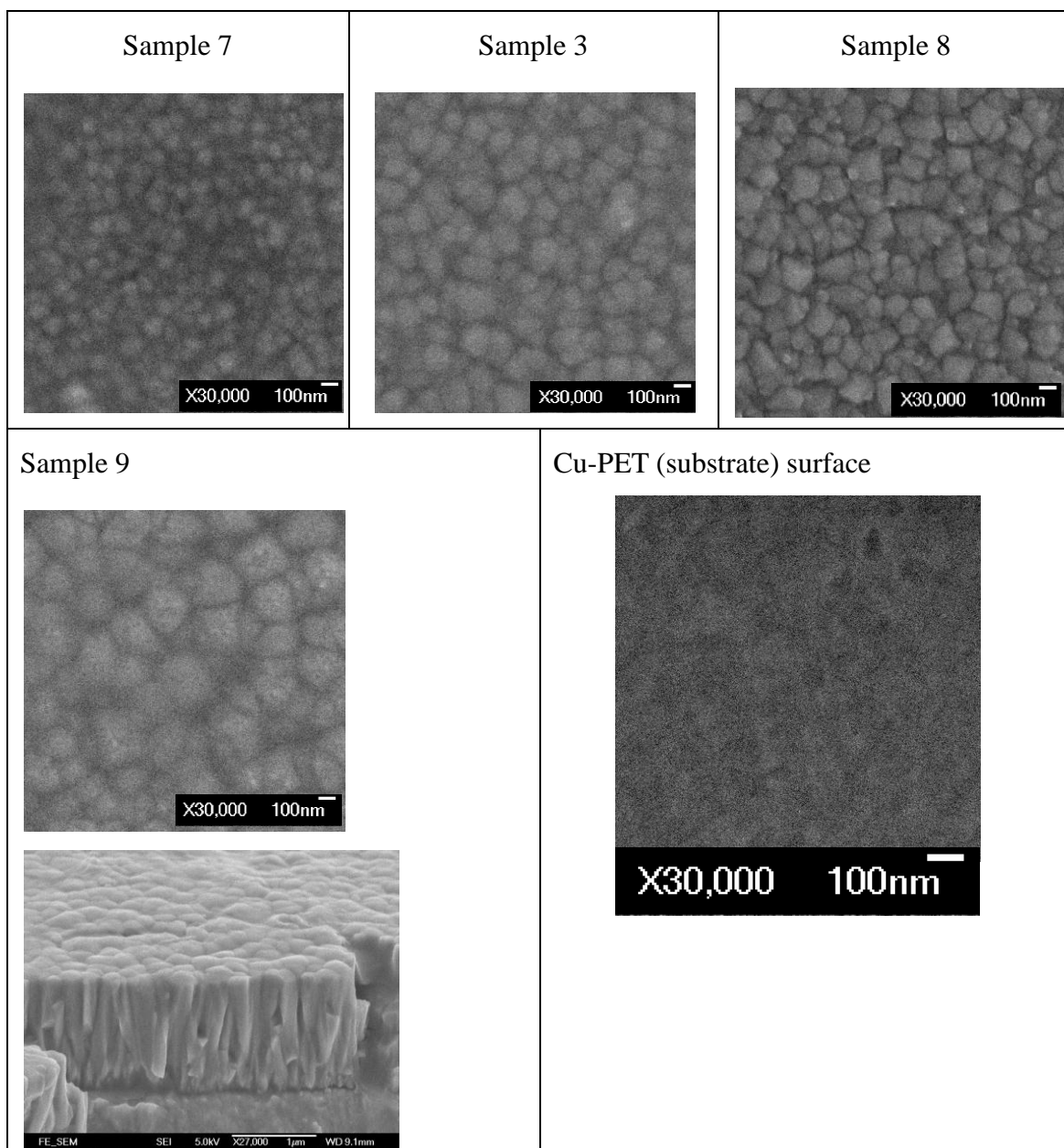
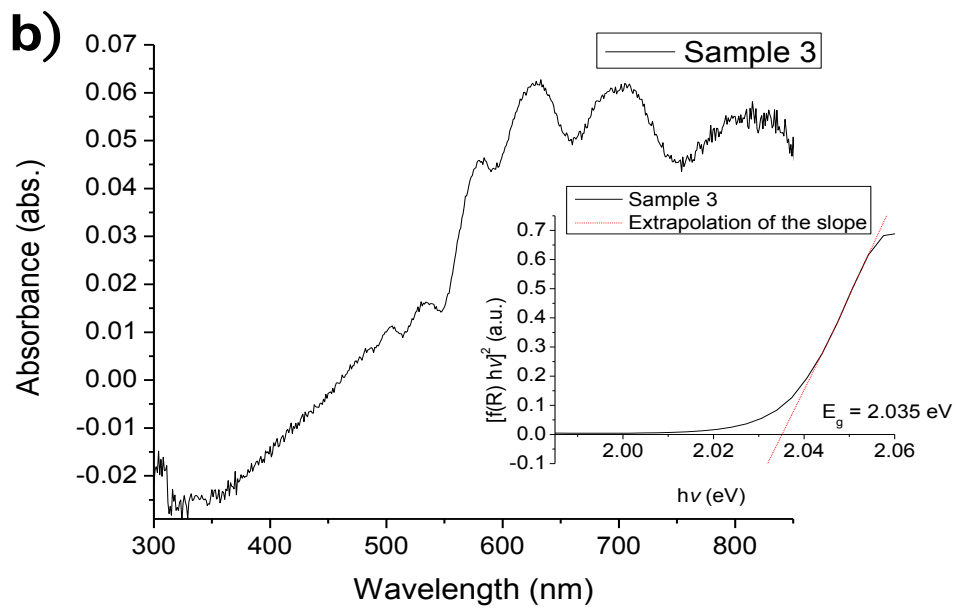
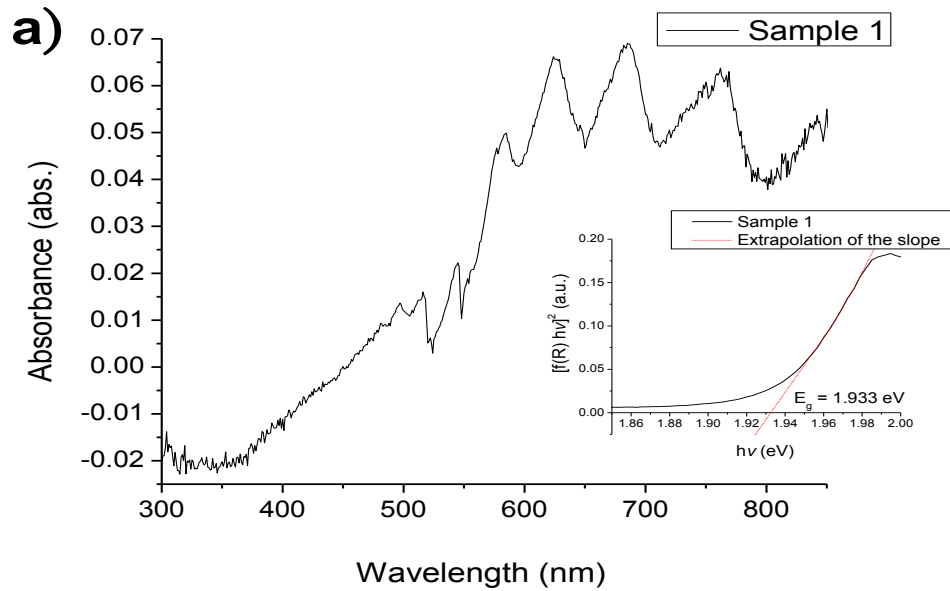


Figure 34 SEM micrographs of the  $\text{Cu}_2\text{O}$  films prepared by different deposition time.

### 4.2.3 Optical Properties



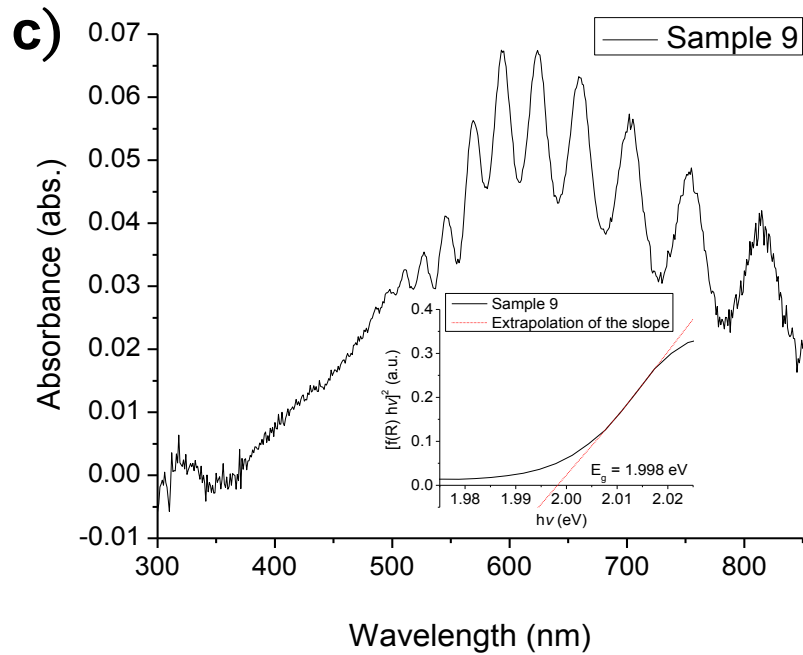


Figure 35 Absorbance of UV-VIS measurement on a) sample 1, b) sample 3 and c) sample 9. Insets show the Kubelka-Munk transformed reflectance spectrum of each sample.

UV-VIS absorption spectra are shown in Figure 35. All the tested samples show oscillations at long wavelength range indicating that the film thicknesses are quite uniform with flat surfaces and sharp interfaces, the observed absorption edges of sample 1, sample 3 and sample 9 are around 550nm. The extrapolation of the slope of the Kubelka-Muck transformed reflectance spectra of sample 1, sample 3 and sample 9 intercept the x-axis, which determines the band-gap value of the as-grown films, giving values of 1.93 eV, 2.04 eV and 2.00 eV, respectively. The results are in good agreement with literature value of 1.97 eV for Cu<sub>2</sub>O single crystals and consistent with the results from other group.[60, 61]

## 4.2.4 Electrical Properties

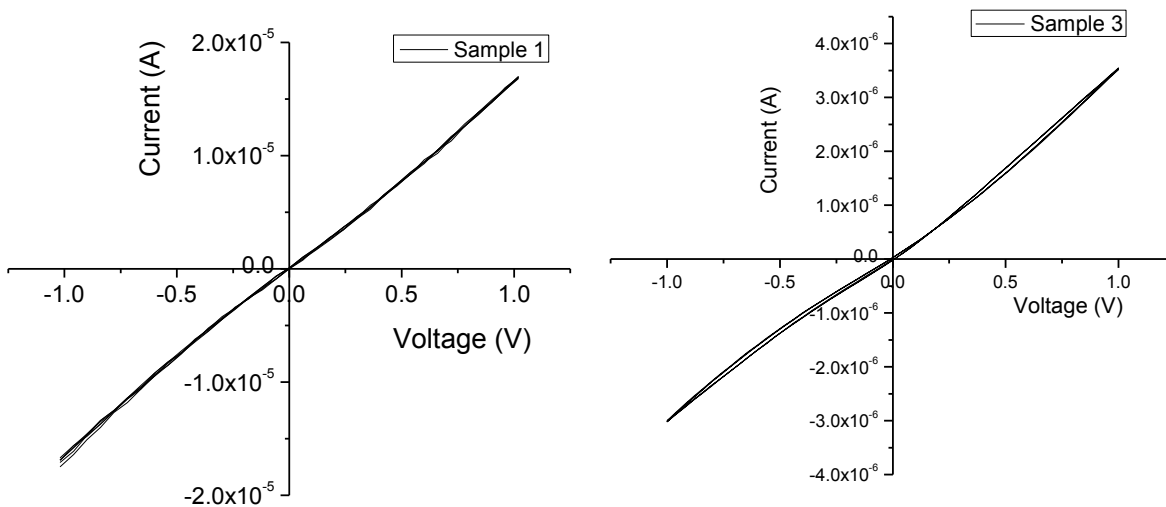


Figure 36 The current-voltage curve of the sample 1 and sample 3.

The resistivity of the films can be calculated through the following equation:

$$\rho = \frac{RA}{L}$$

For sample 1, the area (A) of platinum electrode is  $0.025 \text{ cm}^2$ , the film thickness (L) estimated through dividing the mass per unit area by the density of  $\text{Cu}_2\text{O}$  ( $6.0 \text{ g cm}^{-3}$ ) is 494nm and the resistance (R) obtained from the slope of the curve is  $5 \times 10^4 \Omega$ . For sample 3, the area (A) of platinum electrode is  $0.025 \text{ cm}^2$ , the estimated film thickness (L) is 674nm and the resistance (R) obtained from the slope of the curve is  $3.33 \times 10^5 \Omega$ .

Table 12 shows the resistivity values of the films. Sample 6 has not been studied due to the rough surface which is not favor for the physical deposition of top electrode. Sample 7 has also not been studied because the electrodeposited film with thickness of 343nm does not completely cover the Cu-coated substrate, a direct contact between

a top electrode and the substrates is found.

Sample	Area of electrode (cm <sup>2</sup> )	The calculated Thickness (nm)	R (Ω)	$\rho$ (Ω-cm)
1	0.0025	494	$5 \times 10^4$	$2 \times 10^6$
2	0.0025	612	$1 \times 10^5$	$4 \times 10^6$
3	0.0025	647	$3 \times 10^5$	$1 \times 10^7$
4	0.0025	1333	$5 \times 10^5$	$9 \times 10^6$
5	0.0025	6062	$1 \times 10^4$	$6 \times 10^4$
6	-	-	-	-
7	-	-	-	-
8	0.0025	1168	$1 \times 10^7$	$3 \times 10^8$
9	0.0025	1919	$3 \times 10^7$	$4 \times 10^8$

Table 12. Table showing the resistivity of different Cu<sub>2</sub>O films.

The calculated resistivity of sample 1 and sample 3 are  $2.53 \times 10^6 \Omega\text{-cm}$  and  $1.24 \times 10^7 \Omega\text{-cm}$  respectively. These values are close to the reported values from other groups.[62, 63] Moreover, both cuprous oxide layers show ohmic contacts between the

deposited metal. The resistivity of sample 1 is an order less than that of sample 3 due to less grain boundaries inside, as a slower growth rate usually produce a more regular crystal structure. Thus, the electron mobility is higher in sample 1. Increasing applied voltage does not change the resistivity too much, where sample 1 to sample 4 posses the resistivity of  $\sim 10^6$  to  $10^7 \Omega\text{-cm}$ . For the sample 5, the dramatic drop of resistivity to  $10^4 \Omega\text{-cm}$  might be accounted by the co-deposition of Cu metal into the films due to a high deposition voltage. When low resistance Cu metal is incorporated in the  $\text{Cu}_2\text{O}$  films, the electric current can bypass the high resistance  $\text{Cu}_2\text{O}$  grains. As a result, the resistivity of sample 5 diminishes when compared with other  $\text{Cu}_2\text{O}$  layer of films. The samples 8 and 9 exhibit a higher resistivity of  $10^8 \Omega\text{-cm}$ . They are still in the range of values reported for  $\text{Cu}_2\text{O}$  films prepared by chemical bath deposition and thermal oxidation. This is properly because a longer deposition period lead to the formation of defects. Hence, the electrons will be localized and trapped thus the mobility of the electrons will be lowered.

Figure 37 shows the photocurrent generated when a light source is illuminated on the photoelectrochemical cell using sample 3 as the working electrode. When the light is illuminated onto the surface of  $\text{Cu}_2\text{O}$  layer, electron hole pairs are generated from the surface and thus a cathodic current is generated. Referring to chapter 2.6, the cuprous

oxide produced through this method should be a p-type conducting semiconductor. Illumination of the semiconductor causes a dramatic increase of the concentration of minority carriers, which are electrons in a p-type semiconductor. The electric field drives the photo generated minority carriers towards the semiconductor/liquid interface, where they may participate in the electrochemical reactions occurred in the solution with a suitable redox species. Thus a p-type  $\text{Cu}_2\text{O}$  semiconductor is capable of reducing more species under illumination than in the dark, causing an increase of cathodic current while the anodic current remains unaffected.

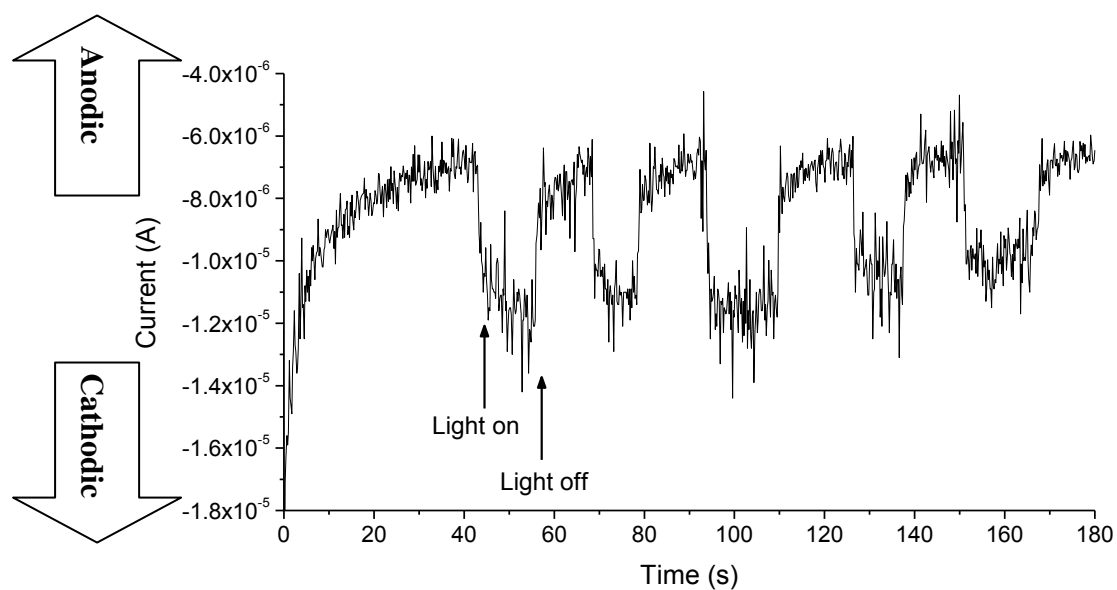


Figure 37 Current-potential characteristics for a  $\text{Cu}_2\text{O}$  layer of sample 3 under and without illumination in 0.5 M  $\text{NaHCO}_3$  solution.

## 4.3 Hetero-Junction of Zinc Oxide / Cuprous Oxide

### 4.3.1 Electrodeposition

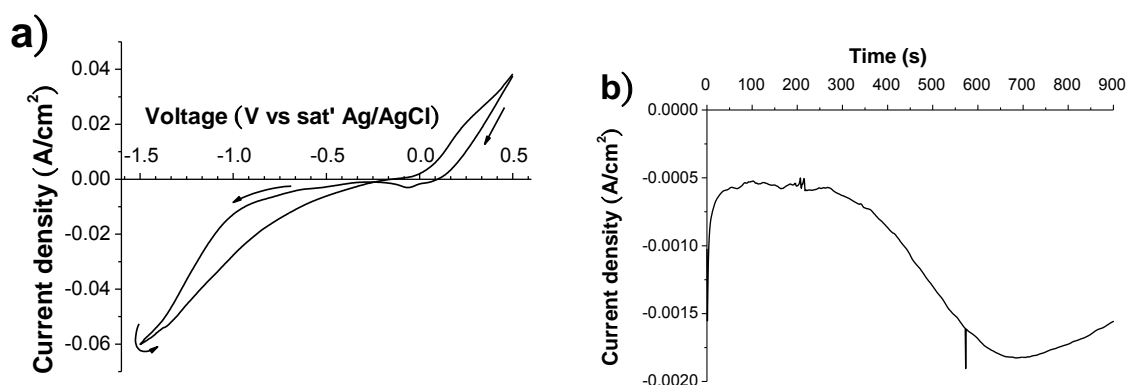


Figure 38 a) cyclic voltammogram of a  $\text{Cu}_2\text{O}$  film electrode (sample 1 was used) in 0.1M zinc nitrate bath with bath temperature of  $80^\circ\text{C}$  and pH of 3.6. b) current transient curve during the potentiostatic deposition at -0.55V.

The processing characteristics of a 0.1M zinc nitrate bath on the sample 1 is shown in figure 38. In figure 38a, the cyclic voltammogram ramps from 0.5V to -1.5V and then returns to 0.5V again. As the cathodic voltage varies between -0.25V and -1.0V, a flat current density is obtained. This corresponds to the reduction of nitrate ions. Then a steep increase in cathodic current appears due to the reduction of zinc ions to zinc metals. In comparison with the voltammograms obtained from ZnO film on Cu/PET, the crossover is located at a more positive side, so the nucleation can be achieved by

applying a relatively low deposition potential.

Figure 38b shows the deposition rate during the potentiostatic deposition. The reaction rate is maintained at  $-0.5 \text{ mA cm}^{-2}$  for the first 5 minutes, and then it reaches a minimum of about  $-1.8 \text{ mA cm}^{-2}$  at 650s. Benefit from the bottom ZnO seed layer, which nucleated during the first 5 minutes, the growth rate increases as less energy is needed for the growth of the top ZnO layer.

### 4.3.2 Structural Properties

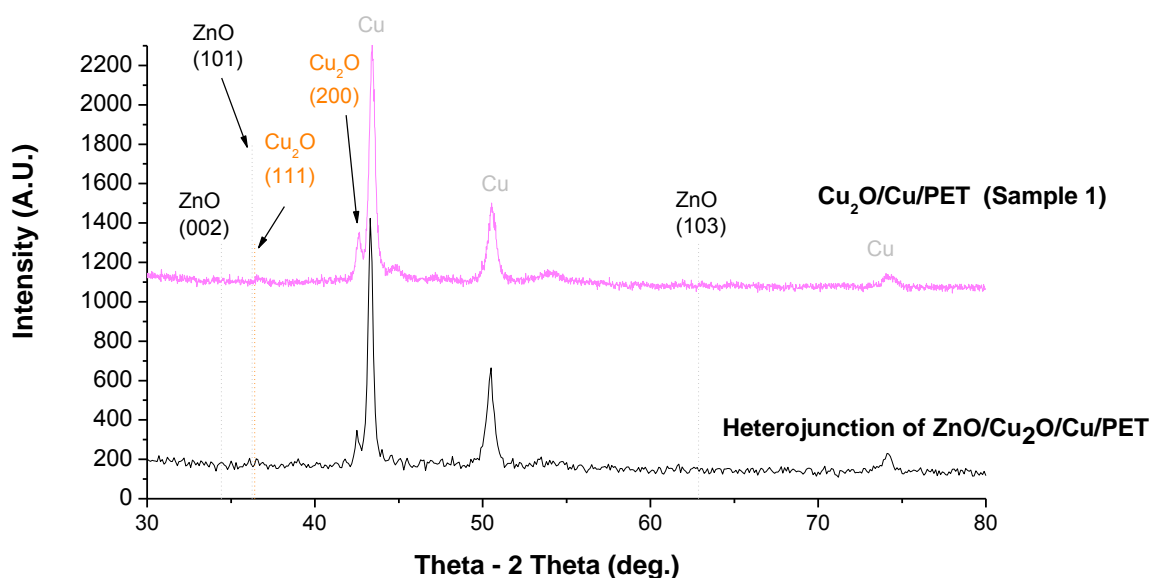


Figure 39 XRD patterns of sample 1 before (upper) and after (lower) the fabrication of a ZnO layer on it.

Structural characterization of the deposited ZnO/Cu<sub>2</sub>O films were obtained by X-ray diffraction measurement. However, no diffraction peaks from the ZnO layer were

observed. One of the possible reasons is that the as grown ZnO layer is too thin and/or the zinc oxide formed might be amorphous instead of polycrystalline.

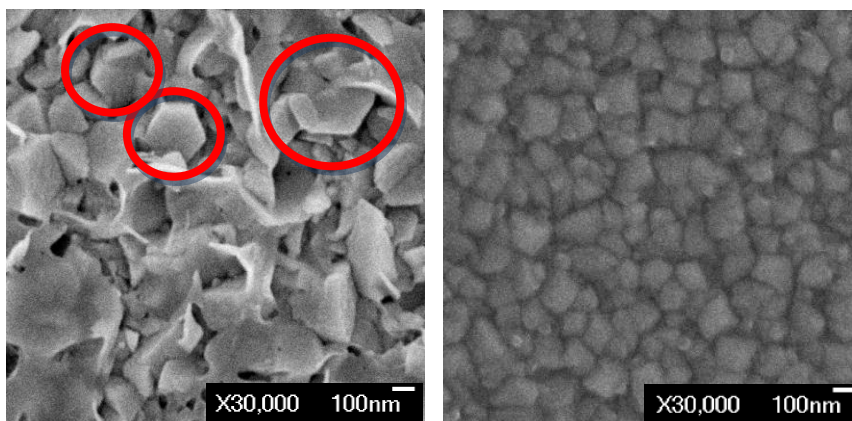


Figure 40 The SEM image shows the surface of the ZnO electrodeposited on cuprous oxide layer (left) and the sample 1 (right).

SEM was employed to reveal the surface morphology of the heterjunction. Figure 40 shows the SEM micrograph of the film. It clearly shows that some hexagonal grains (highlighted with red circles) of size  $\sim 200\text{nm}$ , which are the characteristic feature of ZnO, randomly sit on the sample. Beside these well defined size grains, grains of irregular shape are also observed. Therefore, it is believed that the potentiostatic deposited zinc oxide might exist in the form of amorphous form.

### 4.3.3 Optical Properties

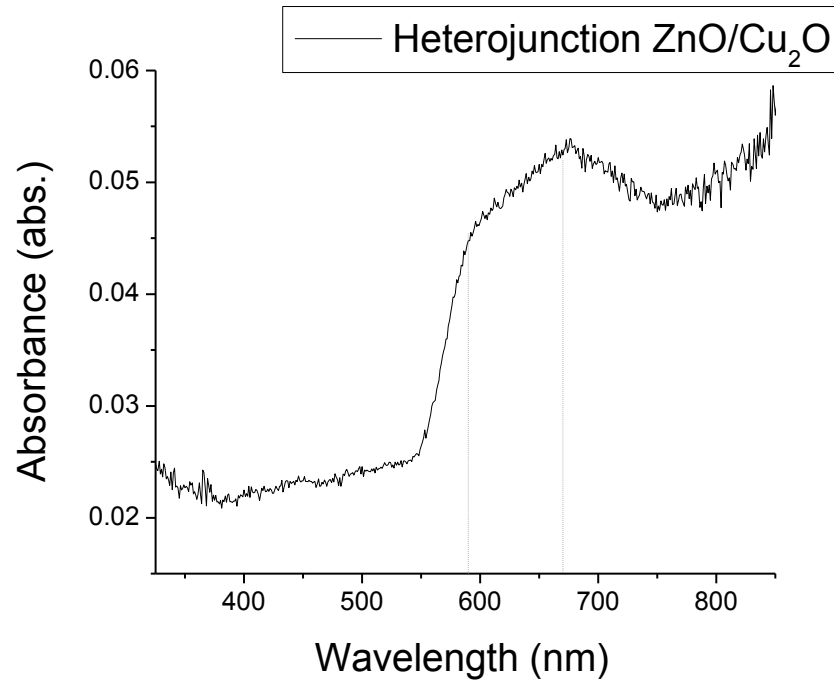


Figure 41 The UV-VIS reflectance of the ZnO/Cu<sub>2</sub>O sample represents in terms of absorbance versus the wavelength.

In figure 41, the UV-VIS reflectance spectrum recorded a gradually drop of reflectance at 670nm and absorption edge is located at 590nm which is very similar to the absorbance of Cu<sub>2</sub>O layers obtained in figure 34. Since the band gap energy of ZnO film is higher than that of the Cu<sub>2</sub>O layer, thus the reflectance spectrum is dominant by the bottom Cu<sub>2</sub>O layer. It is important for the heterojunction to be useful as an optoelectronic device that the Cu<sub>2</sub>O under layer can still absorb the light from front side.

### 4.3.4 Electrical Properties

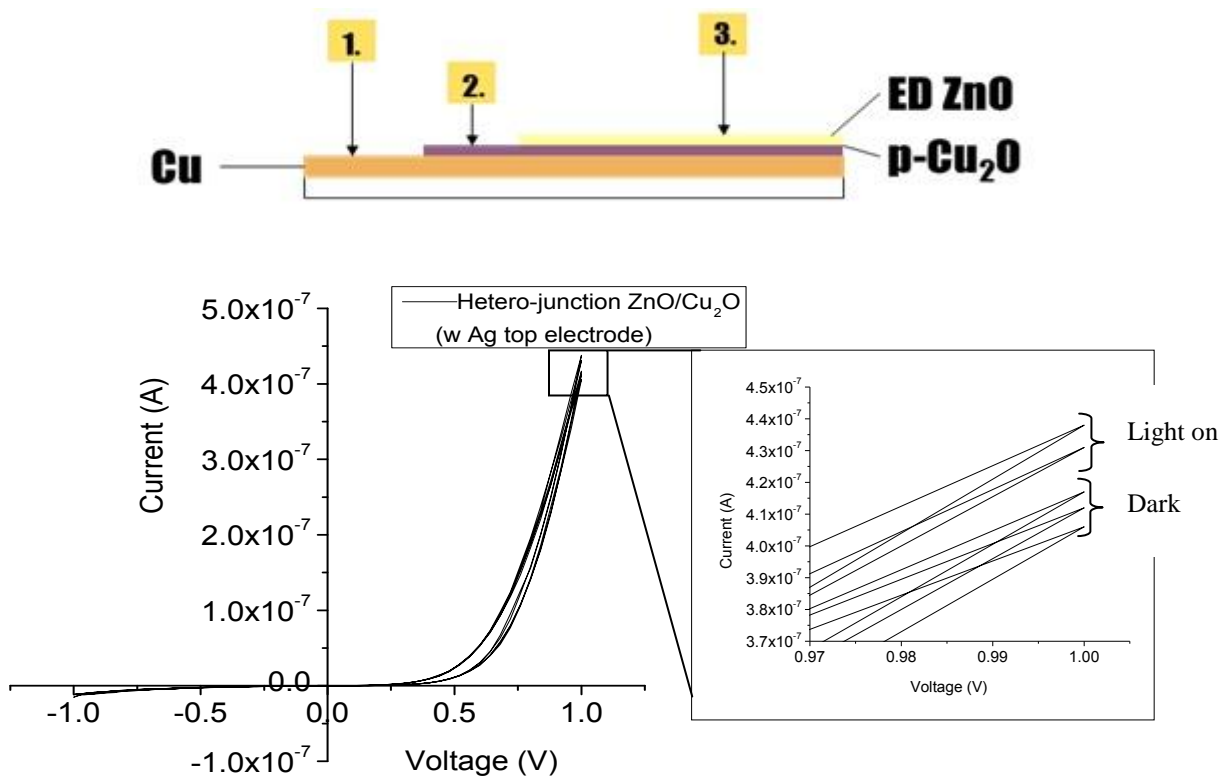


Figure 42 The current-voltage curve of the deposited ZnO/Cu<sub>2</sub>O heterojunction.

The electrical characteristic of this electrodeposited ZnO/Cu<sub>2</sub>O heterojunction is shown in figure 42. The current-voltage curve shows a typical rectifying profile for this contact, which is a fundamental property of a p-n junction. Since the ZnO and Cu<sub>2</sub>O show a n-type and p-type conductivity respectively, the contact of this junction is expected to perform a rectifying signal. However, the magnitude of current response to the voltage is very low ( $10^{-7}$  A). The inset of figure 42 shows that this junction also responds to light illuminated on the sample. The light used in this experiment was a

white light emitting diode. As seen in the figure, when the light was on, the current increased.

The built-in potential for the sample shown in Fig. 42 could be estimated to be about 0.7 eV, where the built-in potential is predicted to be  $\sim 1.0$  eV for the ideal case.[32, 64]

In the absence of defect states, the built-in potential for heterojunctions is equal to the difference in the work function between two semiconductors. Fig. 43 shows the both the isolated states and the junction of ZnO and  $\text{Cu}_2\text{O}$ . The smaller value of the built-in potential may be possibly due to residual defect states and impurity amounts.[65] It is necessary to optimise the layered structure and their carrier concentrations to obtain better  $I-V$  characteristics.

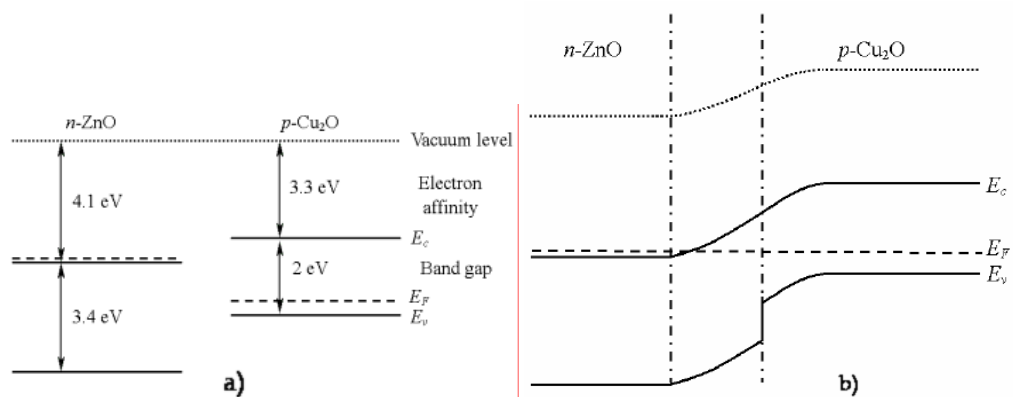


Figure 43 Band diagrams of the isolated states (a) and the junction of ZnO and  $\text{Cu}_2\text{O}$  (b).[64, 66]  $E_C$ ,  $E_V$  and  $E_F$  are the conduction-band-edge, valence-band-edge and Fermi-level, respectively.

## Chapter 5 Conclusion

ZnO thin films have been successfully deposited on flexible substrates using potentiostatic cathodic deposition method. XRD patterns reveal that highly c-axis oriented crystalline films are obtained under most of the fabrication conditions. SEM microstructural studies show that nanorods, nanoplatelet and dense thin films of ZnO are obtained depending on the process parameters. Photoluminescence spectra reveal the presence of oxygen interstitials in the films due to the observation of yellow emissions. An UV-Vis reflectance spectrum indicates a bandgap energy of 3.23eV. Our results demonstrate that high quality ZnO films can be grown on flexible polymeric surface using potentiostatic cathodic deposition technique.

On the other hand, Cu<sub>2</sub>O thin films have also been successfully deposited on copper coated PET substrates. Crystal orientations of (111) and (200) are dominated at high deposition voltage and low deposition voltage respectively where the structural properties and surface morphology of the films do not show a large dependency on the deposition time. Similar to ZnO films, electrodeposited Cu<sub>2</sub>O films absorb photons with wavelength shorter than 550nm due to their bandgap. The electrodeposited cuprous oxide thin film possess a p-type conductivity with resistivity

in an order of  $10^6 \sim 10^7 \Omega \text{ cm}$ . Electrodeposition and characterization of the heterostructure proved that further optimization of the processing condition is required since amorphorous ZnO layers are formed and this results in a very low current response to light. In the future, different dopants should be added into the film for lowering the resistivity of  $\text{Cu}_2\text{O}$  which is important for a high efficiency solar cell material. In order to use  $\text{Cu}_2\text{O}$  and ZnO in future photovoltaic device applications, it is worth to continue the research on these two materials.

To improve the photovoltaic performance, a detail study should be focus on the reduction of the resistivity of the  $\text{Cu}_2\text{O}$  films through doping. Furthermore, the oxide film thickness should be optimized so that it can be bent without cracking as a practical flexible electronic device.

## Reference

1. Surek, T., *Crystal growth and materials research in photovoltaics: progress and challenges*. Journal of Crystal Growth, 2005. **275**(1/2): p. 292-304.
2. Kazmerski, L., *NREL Compilation of best research solar cell efficiencies*, N.R.E.L. (NREL), Editor. 2010: Golden, Colorado.
3. Schubert, M.B. and R. Merz, *Flexible solar cells and modules*. Philosophical Magazine, 2009. **89**(28-30): p. 2623-2644.
4. Dae-Hyeong, K., et al., *Stretchable and Foldable Silicon Integrated Circuits*. Science, 2008. **320**(5875): p. 507-511.
5. Kessler, F., D. Herrmann, and M. Powalla, *Approaches to flexible CIGS thin-film solar cells*. Thin Solid Films, 2005. **480-481**: p. 491-498.
6. Hartmann, M., et al. *Flexible and light weight substrates for Cu(In,Ga)Se<sub>2</sub> solar cells and modules*. in *Photovoltaic Specialists Conference, 2000. Conference Record of the Twenty-Eighth IEEE*. 2000.
7. Danaher, W.J. and L.E. Lyons, *Photoelectrochemical cell with cadmium telluride film*. Nature, 1978. **271**(5641): p. 139-139.
8. Fulop, G.F. and R.M. Taylor, *ELECTRODEPOSITION OF SEMICONDUCTORS*. Annual Review of Materials Science, 1985. **15**: p. 197-210.
9. Basol, B.M., *HIGH-EFFICIENCY ELECTROPLATED HETEROJUNCTION SOLAR-CELL*. Journal of Applied Physics, 1984. **55**(2): p. 601-603.
10. Nohira, T., K. Yasuda, and Y. Ito, *Pinpoint and bulk electrochemical reduction of insulating silicon dioxide to silicon*. Nature Materials, 2003. **2**(6): p. 397-401.
11. Griffiths, L.E., et al., *Low temperature electrochemical synthesis of titanium nitride*. Chemical Communications, 2001(6): p. 579-580.
12. Ramamoorthy, K., et al., *Development of a novel high optical quality ZnO thin films by PLD for III-V opto-electronic devices*. Current Applied Physics, 2006. **6**(1): p. 103-108.
13. Wu, S., et al., *Improvement in dye-sensitized solar cells with a ZnO-coated TiO<sub>2</sub> electrode by rf magnetron sputtering*. Applied Physics Letters, 2008. **92**(12): p. 122106-122106-3.
14. De Vittorio, M., et al., *Nano-island fabrication by electron beam lithography and selective oxidation of Al-rich AlGaAs layers for single electron device application*. Microelectronic Engineering, 2002. **61-62**: p. 651-656.
15. Fragalà, M.E., et al., *Colloidal lithography and Metal-Organic Chemical Vapor Deposition process integration to fabricate ZnO nanohole arrays*. Thin

- Solid Films, 2010. **518**(16): p. 4484-4488.
16. Jin, Z., et al., *High throughput fabrication of transition-metal-doped epitaxial ZnO thin films: A series of oxide-diluted magnetic semiconductors and their properties*. Applied Physics Letters, 2001. **78**(24): p. 3824-3826.
  17. Dharmadasa, I.M. and J. Haigh, *Strengths and Advantages of Electrodeposition as a Semiconductor Growth Technique for Applications in Macroelectronic Devices*. Journal of The Electrochemical Society, 2006. **153**(1): p. G47-G52.
  18. Therese, G.H.A. and P.V. Kamath, *Electrochemical Synthesis of Metal Oxides and Hydroxides*. Chemistry of Materials, 2000. **12**(5): p. 1195-1204.
  19. Bunn, C.W., *The lattice-dimensions of zinc oxide*. Proceedings of the Physical Society, 1935. **47**(5): p. 835.
  20. Ozgur, U., et al., *A comprehensive review of ZnO materials and devices*. Journal of Applied Physics, 2005. **98**(4): p. 041301-103.
  21. Look, D.C., et al., *Electrical properties of bulk ZnO*. Solid State Communications, 1998. **105**: p. 399-401.
  22. Segawa, Y., et al., *Growth of ZnO Thin Film by Laser MBE: Lasing of Exciton at Room Temperature*. physica status solidi (b), 1997. **202**(2): p. 669-672.
  23. Markevich, I.V., et al., *Centers of photosensitivity in ZnO*. Solid State Communications, 2007. **144**(5-6): p. 236-239.
  24. Rai, B.P., *Cu<sub>2</sub>O solar cells: A review*. Solar Cells, 1988. **25**(3): p. 265-272.
  25. Biccari, F., C. Malerba, and A. Mittiga, *Chlorine doping of Cu<sub>2</sub>O*. Solar Energy Materials and Solar Cells, 2010. **94**(11): p. 1947-1952.
  26. Siripala, W. and J.R.P. Jayakody, *Observation of n-type photoconductivity in electrodeposited copper oxide film electrodes in a photoelectrochemical cell*. Solar Energy Materials, 1986. **14**(1): p. 23-27.
  27. Jayewardena, C., et al., *Fabrication of n-Cu<sub>2</sub>O electrodes with higher energy conversion efficiency in a photoelectrochemical cell*. Solar Energy Materials and Solar Cells, 1998. **56**(1): p. 29-33.
  28. Fernando, C.A.N. and S.K. Wetthasinghe, *Investigation of photoelectrochemical characteristics of n-type Cu<sub>2</sub>O films*. Solar Energy Materials and Solar Cells, 2000. **63**(3): p. 299-308.
  29. Garuthara, R. and W. Siripala, *Photoluminescence characterization of polycrystalline n-type Cu<sub>2</sub>O films*. Journal of Luminescence, 2006. **121**(1): p. 173-178.
  30. Scanlon, D.O. and G.W. Watson, *Undoped n-Type Cu<sub>2</sub>O: Fact or Fiction?* The Journal of Physical Chemistry Letters, 2010. **1**(17): p. 2582-2585.
  31. Wang, L. and M. Tao, *Fabrication and Characterization of p-n Homojunctions*

- in Cuprous Oxide by Electrochemical Deposition*. Electrochemical and Solid-State Letters, 2007. **10**(9): p. H248-H250.
32. Masanobu, I. and et al., *Electrochemically constructed p-Cu<sub>2</sub>O/n-ZnO heterojunction diode for photovoltaic device*. Journal of Physics D: Applied Physics, 2007. **40**(11): p. 3326.
  33. Jeong, S.S., et al., *Electrodeposited ZnO/Cu<sub>2</sub>O heterojunction solar cells*. Electrochimica Acta, 2008. **53**(5): p. 2226-2231.
  34. Musselman, K.P., et al., *A Novel Buffering Technique for Aqueous Processing of Zinc Oxide Nanostructures and Interfaces, and Corresponding Improvement of Electrodeposited ZnO-Cu<sub>2</sub>O Photovoltaics*. Advanced Functional Materials, 2010: p. n/a-n/a.
  35. Trivich, D., et al., *CUPROUS OXIDE PHOTOVOLTAIC CELLS*. Conference Record of the IEEE Photovoltaic Specialists Conference, 1978: p. 174-179.
  36. Rakhshani, A.E., *PREPARATION, CHARACTERISTICS AND PHOTOVOLTAIC PROPERTIES OF CUPROUS-OXIDE - A REVIEW*. Solid-State Electronics, 1986. **29**(1): p. 7-17.
  37. R.K. Pandey, S.N.S., S. Chandra, *Handbook of semiconductor electrodeposition*. 1996, New York: Marcel Dekker.
  38. Donald T. Sawyer, A.S., Julian L. Roberts, Jr, *Electrochemistry for chemists*. 1995, New York: Wiley.
  39. Tan, L., Nguyen, Kesselman, Stanton, & Lewis 1994. Tan, M. X., Laibinis, P. E., Nguyen, S. T., Kesselman, J. M., Stanton, C. E., & Lewis, N. S., *Principles and applications of semiconductor photoelectrochemistry*. Progress in inorganic chemistry, 1994. **41**.
  40. Siripala, W., et al., *Band edge shifts of p-type copper indium diselenide electrodes in aqueous electrolytes*. Applied Physics Letters, 1993. **62**(5): p. 519-521.
  41. Deen, M. and F. Pascal, *Electrical characterization of semiconductor materials and devices—review*. Journal of Materials Science: Materials in Electronics, 2006. **17**(8): p. 549-575.
  42. Pierret, R., *Modular Series on Solid State Devices*. Advance Semiconductor Fundamentals. Vol. 6. 1987: Addison-Wesley.
  43. Tandon, S.P. and J.P. Gupta, *Diffuse Reflectance Spectrum of Cuprous Oxide*. physica status solidi (b), 1970. **37**(1): p. 43-45.
  44. Mahalingam, T., et al., *Electrodeposition and characterization of transparent ZnO thin films*. Solar Energy Materials and Solar Cells, 2005. **88**(2): p. 227-235.
  45. Shang, W., et al., *Growth and characterization of electro-deposited Cu<sub>2</sub>O and*

- Cu thin films by amperometric I-T method on ITO/glass substrate.* Applied Physics A: Materials Science & Processing, 2007. **87**(1): p. 129-135.
46. Wu, L., et al., *Photoelectrochemical Stability of Electrodeposited Cu<sub>2</sub>O Films.* The Journal of Physical Chemistry C, 2010. **114**(26): p. 11551-11556.
  47. Liu, H., et al., *Electrochemical impedance spectroscopy of ZnO nanostructures.* Electrochemistry Communications, 2009. **11**(5): p. 945-949.
  48. Inamdar, A.I., et al., *Electrodeposited zinc oxide thin films: Nucleation and growth mechanism.* Solar Energy Materials and Solar Cells, 2007. **91**(10): p. 864-870.
  49. Vanýsek, P., *Electrochemical Series*, in *Handbook of Chemistry and Physics: 91<sup>th</sup> Edition*, W.M.M. Haynes, Editor. 2010, Taylor and Francis Group, LLC. p. 20-29.
  50. Heerman, L. and A. Tarallo, *Theory of the chronoamperometric transient for electrochemical nucleation with diffusion-controlled growth.* Journal of Electroanalytical Chemistry, 1999. **470**(1): p. 70-76.
  51. Pauporté, T. and D. Lincot, *Electrodeposition of semiconductors for optoelectronic devices: results on zinc oxide.* Electrochimica Acta, 2000. **45**(20): p. 3345-3353.
  52. Li, W.-J., et al., *Growth mechanism and growth habit of oxide crystals.* Journal of Crystal Growth, 1999. **203**(1-2): p. 186-196.
  53. Laurent, K., et al., *Structural and optical properties of electrodeposited ZnO thin films.* Thin Solid Films, 2008. **517**(2): p. 617-621.
  54. Huang, K., et al., *Photoluminescence oscillations in porous alumina films.* Applied Physics Letters, 2006. **89**(20): p. 201118-3.
  55. Li, Q.H., et al., *Oxygen sensing characteristics of individual ZnO nanowire transistors.* Applied Physics Letters, 2004. **85**(26): p. 6389-6391.
  56. Chang, P.C., et al., *ZnO nanowires synthesized by vapor trapping CVD method.* Chemistry of Materials, 2004. **16**(24): p. 5133-5137.
  57. Poizot, P., et al., *An electrochemical method for CuO thin film deposition from aqueous solution.* Electrochemical and Solid State Letters, 2003. **6**(2): p. C21-C25.
  58. White, R.E., *Experimental methods in electrochemistry.* 1984, New York: Plenum Press.
  59. Group., S.E., *Instrumental methods in electrochemistry.* 1985, New York: Wiley.
  60. Mahalingam, T., et al., *Structural and annealing studies of potentiostatically deposited Cu<sub>2</sub>O thin films.* Solar Energy Materials and Solar Cells, 2005. **88**(2): p. 209-216.

61. Guillén, C. and J. Herrero, *Optical properties of electrochemically deposited CuInSe<sub>2</sub> thin films*. Solar Energy Materials, 1991. **23**(1): p. 31-45.
62. Mahalingam, T., et al., *Preparation and microstructural studies of electrodeposited Cu<sub>2</sub>O thin films*. Materials Letters, 2004. **58**(11): p. 1802-1807.
63. McShane, C.M., W.P. Siripala, and K.-S. Choi, *Effect of Junction Morphology on the Performance of Polycrystalline Cu<sub>2</sub>O Homojunction Solar Cells*. The Journal of Physical Chemistry Letters, 2010. **1**(18): p. 2666-2670.
64. Ishizuka, S., et al., *Polycrystalline n-ZnO/p-Cu<sub>2</sub>O heterojunctions grown by RF-magnetron sputtering*. physica status solidi (c), 2004. **1**(4): p. 1067-1070.
65. Paul, G.K., et al., *Defects in Cu<sub>2</sub>O studied by deep level transient spectroscopy*. Applied Physics Letters, 2006. **88**(14): p. 141901-3.
66. Lv, P., et al., *I-V characteristics of ZnO/Cu<sub>2</sub>O thin film n-i-p heterojunction*. Physica B: Condensed Matter, 2011. **406**(6-7): p. 1253-1257.